Journal of Chemistry

WILEY

RESEARCH ARTICLE OPEN ACCESS

Synergistic Corrosion Inhibition of API 5L X65 Steel by Phytochemical Extracts: A Multitechnique Approach With Computational Validation

Joseph Itodo Emmanuel[1] | Odette Fayen Ngasoh[2] | Abdulhakeem Bello[3] | Vitalis Chioh Anye[2] | Chidiebele E. J. Uzoagba[4] | Azikiwe Peter Onwualu[1] | Yashwansingh Baboo Surnam[5]

[1]Materials Science & Engineering, African University of Science & Technology Abuja, Galadima, Nigeria | [2]Mechanical, Materials Engineering, African University of Science & Technology Abuja, Galadima, Nigeria | [3]Theoretical, Applied Physics, African University of Science & Technology Abuja, Galadima, Nigeria | [4]Petroleum and Energy Resources Engineering, African University of Science & Technology Abuja, Galadima, Nigeria | [5]Faculty of Engineering, University of Mauritius, Reduit, Moka 80837, Mauritius

Correspondence: Joseph Itodo Emmanuel (jitodo@student.aust.edu.ng)

Received: 25 July 2025 | **Revised:** 31 October 2025 | **Accepted:** 2 January 2026

Academic Editor: Munmun Bardhan

Keywords: computational studies | electrochemical studies | gravimetric analysis | inhibitors | phytochemicals | synergistic interactions

ABSTRACT

The synergistic corrosion inhibition of nine phytochemicals from *Azadirachta indica* (neem) and *Dypsis lutescens* (golden palm) on API 5L X65 steel in acidic media was studied using DFT, MC, weight loss, EIS, and Tafel (PDP) methods, supported by FE-SEM and EDX analyses. Quantum chemical parameter analysis indicated synergistic interactions among the phytochemicals via nucleophilic and electrophilic attacks. The orbital matching principle revealed electron donation from the HOMO of 6,11-dimethyl-2,6,10-dodecatrien-1-ol, methyl ester (Z), D-limonene, and 9-eicosene to the iron Fermi level (−5.177 eV), due to small energy gaps (0.625, 0.738, and −0.249 eV). Electron transfer from the Fermi level of Fe to the LUMO of 9-eicosene is favored. The remaining six phytochemicals exhibited high hardness and enhanced stability. MC simulations showed an adsorption energy of −4472.220 kcal/mol. The weight loss indicated that GT 85 achieved inhibition efficiencies of 72% at 303 K, 88% at 314 K, and 94% at 328 K after 24 h. The EIS and PDP results showed efficiencies of 94.79 ± 0.0281 and 99.9%, respectively. The Nyquist plots indicate an activation-controlled mechanism with an increased charge transfer resistance from 2.401 ± 0.032 $\Omega \cdot cm^2$ (blank) to 46.103 ± 0.357 $\Omega \cdot cm^2$ at 60 ppm. FE-SEM and EDX confirmed the GT 85 protective film. The adsorption process of GT 85 followed the Langmuir and Freundlich isotherms, and thermodynamic analysis revealed a spontaneous physisorption mechanism. The results revealed that GT 85 is thermally stable up to 328 K, anodic, persistent, and effective at low dosages and offers an eco-friendly alternative green inhibitor with minimal environmental impact.

Research Highlights

- GT 85 inhibited the acidic corrosion of API 5L X65 steel, achieving 99.9% inhibition efficiency (IE) by Tafel plots and 94% by weight loss (WL) at 328 K over 24 h.
- DFT and MC showed that all nine phytochemicals in GT 85 interacted synergistically, resulting in strong adsorption on the Fe (111) crystal surface.
- GT 85 is thermally stable up to 328 K, anodic, persistent, and effective at low concentrations.

This is an open access article under the terms of the Creative Commons Attribution License, which permits use, distribution and reproduction in any medium, provided the original work is properly cited.

Copyright © 2026 Joseph Itodo Emmanuel et al. *Journal of Chemistry* published by John Wiley & Sons Ltd.

1 | Background

Corrosion of engineering materials in acidic and other harsh environments is a major challenge in the oil, gas, and related industries [1]. Oil and gas production fluids are highly corrosive due to the combined effects of stress, temperature, pressure, low pH, dissolved oxygen, sulfate-reducing bacteria, iron-oxidizing bacteria, hydrogen sulfide, carbon dioxide, salts, and organic acids [2–6]. To mitigate internal corrosion in API 5L X65 pipelines and other steel grades, operators use chemical treatment, scheduled dewatering, pipe cleaning, and intelligent pigging [7–9]. The Association of Materials Performance and Protection (AMPP), formerly NACE, and the scientific literature emphasize the urgent need for better corrosion control methods, given the global corrosion cost of approximately $2.5 trillion [7, 9–14].

Traditional corrosion inhibitors, both organic and inorganic, have been effective but are often toxic and bioaccumulative, driving interest in organic green corrosion inhibitors (OGCIs) from plant extracts [1, 3, 8, 9, 14–16]. OGCIs are nontoxic, environmentally friendly, and can replace banned synthetic inhibitors. Raw extracts from *Azadirachta indica* (neem) and *Dypsis lutescens* (golden palm) showed high inhibition efficiency (IE) in various environments [3, 14]. Although some studies have examined their corrosion inhibition properties, few have explored synergistic phytochemical interactions [17–19]. Existing research uses computational tools, such as density functional theory (DFT), Monte Carlo (MC) simulations [1, 20], and material characterization methods [21–25], such as weight loss (WL), potentiodynamic polarization (PDP), and electrochemical impedance spectroscopy (EIS) [12, 25, 26], to evaluate raw extracts. However, significant gaps remain in our understanding of the phytochemical adsorption mechanisms and synergistic effects at the molecular level [14, 27–32]. The numerous phytochemicals present in these extracts complicate the study of their interaction. There is a critical knowledge gap regarding the synergistic inhibition properties of phytochemicals from these plants, particularly when combined to achieve enhanced effects [29, 32–35]. Most recent studies have focused on raw extracts used with salts [36–41], metal oxides [42–44], or ionic liquids [2, 42, 45, 46] using DFT, MC simulations, EIS, PDP, field emission scanning electron microscopy (FE-SEM), and energy-dispersive X-ray spectroscopy (EDX). The limited understanding of plant-based phytochemical synergies has hindered the development of industrially viable OGCIs. A comprehensive review of the scientific studies on the synergistic interaction between 2024 and 2025 is presented in Appendix A.

This research offers several novel contributions to the field of corrosion science. First, it investigates the synergistic anticorrosion properties of a unique molecular combination of nine phytochemicals, 1-docosene, 6,11-dimethyl-2,6,10-dodecatrien-1-ol, 9-eicosene, 17-pentatriacontene, heptadecyl heptafluorobutyrate, D-limonene, hexadecenoic acid, tetradecanoic acid, and Z-2-octadecen-1-ol derived from neem and golden palm leaves. The study examines their effectiveness on API 5L X65 steel in a simulated two-phase crude oil acidic environment. Second, it innovatively combines DFT analysis of quantum chemical parameters (QCPs) and the orbital matching principle (OMP) to provide a critical, in-depth molecular-level analysis addressing significant research gaps in synergistic corrosion inhibition by plant-based phytochemicals. Finally, the study introduces a novel MC simulation of two-phase crude oil using low-aromatic white spirit (LAWS) with varying concentrations of HCl and water.

2 | Materials and Methods

2.1 | Preparation of Plant Extracts and Soxhlet Extraction

Analytical-grade hydrochloric acid (HCl) and methanol were used to prepare all the reagents. Leaves of *Azadirachta indica* (neem) and *Dypsis lutescens* (golden palm) were collected from the Games Village Flower Garden and authenticated in the AUST Abuja Herbarium. Samples were washed with double-distilled water [47] and shade-dried for 4 weeks. The dried leaves were ground into a fine powder, and 20 g of each sample was used for Soxhlet extraction in methanol. After six reflux cycles, the extraction was stopped, and 30 mL of each crude plant extract was collected and stored at $24 \pm 5°C$.

2.2 | Preparation of API 5L X65 Strip Coupons

API 5L X65 pipeline steel with the following elemental composition by weight (in %): C (0.60), Cr (0.02), Mn (0.20), Nb (0.03), S (0.002), and residual Fe, was cut into strip coupons with a surface area of 15.5 cm^2 for WL studies. For the electrochemical studies, a 1-cm^2 area of the strip coupon served as the working electrode, while the rest was coated with high-build epoxy (HBE) at a nominal dry film thickness (NDFT) of 1.5 mm. The electrode surface was polished with emery paper (600–150 grit) to obtain a mirror-like finish. The coupons were washed with double-distilled water, degreased in ethanol and acetone, and dried in a desiccator according to NACE (AMPP) RP0775-2005.

2.3 | Acidic Media Preparation

The acidic test solution was prepared by adding 10 mL of analytical-grade hydrochloric acid (HCl) to 250 mL of distilled water to obtain a 0.5 M HCl solution. Using this solution, the required concentrations were prepared by pipetting Greentreat (GT) 85 for WL, EIS, and PDP experiments. To prevent cross-contamination, separate pipettes were used at each inhibitor concentration. The detailed research methodology is illustrated in Figure 1.

2.4 | Characterization of the Filtrates

Gas chromatography-mass spectrometry (GC-MS) was used to identify and quantify the phytochemicals present in *Azadirachta indica* (neem) and *Dypsis lutescens* (golden palm) (Appendix B). Fourier-transform infrared spectroscopy (FTIR) was performed on the extracts to detect the functional groups and bonding types in both crude extracts (Appendix C). The dominant phytochemicals present in this plant have been identified by Emmanuel et al. [1].

2.5 | Preparation of GT 85

GT 85 was formulated from raw methanol extracts of *Azadirachta indica* (neem) and *Dypsis lutescens* (golden palm) using DFT and MC simulations to analyze electron donation, stability, and adsorption reinforcement. A specific ratio of both extracts

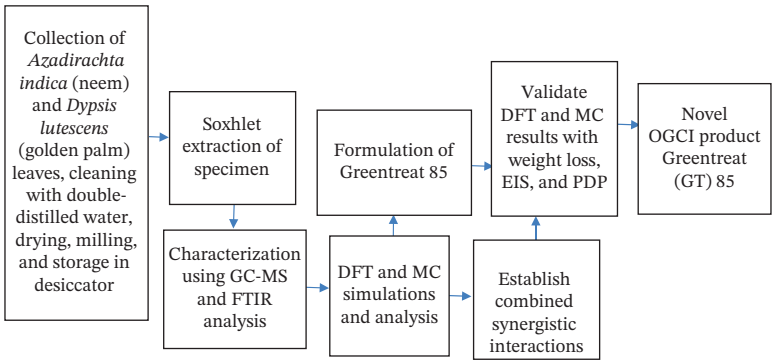


FIGURE 1 | Research methodology.

was used to create the master batch, which was fingerprinted using GC-MS for future product batches. This ensured reproducibility, purity, and standardization. The graphical abstract is provided in Supporting Information (available here).

2.6 | DFT Implantation

Geometry optimization of the nine major phytochemicals was performed using BIOVIA Materials Studio 2020 software in the DMol3 program [29, 31, 48, 49], employing the generalized gradient approximation (m-GGA/M-11L) and double-numeric quality polarization (DNP) at the 3.5 level of theory [34, 50]. The COSMO model was applied to account for the solvent effects by maintaining a continuum solvation model [35]. Undesirable frequencies were eliminated with a self-consistent field (SCF) set at 27e − 5 eV, and the base energy was monitored [48, 51, 52]. A lower convergence criterion of 27e − 5 eV was used to improve the accuracy and ensure sufficient interactions [53, 54].

2.6.1 | QCPs

After obtaining the optimized geometries, the highest occupied molecular orbital (HOMO) and lowest unoccupied molecular orbital (LUMO) were used to calculate other QCPs, including the energy gap (ΔE), dipole moment (p), back-donation (ΔE), global hardness (η), global softness (S or σ), maximum electron charge transfer (ΔN_{max}), and fraction of electrons (ΔN). QCPs were used to predict the corrosion inhibition of phytochemicals based on their electronic structure, stability, and reactivity with the iron surface. These parameters also enabled critical analysis of the synergistic interactions among the nine phytochemicals. The relationships between the QCPs are discussed in the scientific literature [31, 44, 55–60].

2.7 | MC Simulations

The MC simulation technique was used to investigate and predict the anticorrosion properties of phytochemical molecules on the Fe crystal surface [3, 29, 31, 61–63]. The MC simulation of the optimized phytochemical molecules was performed on an Fe (111) unit cell with a thickness of five atoms in acidic media consisting of 30% water cut (21 H_2O, 9 HCl, 70 LAWS), 50% water cut (41% H_2O, 9 HCl, 50 LAWS), and 70% water cut (61% H_2O, 9 HCl, 30 LAWS). A LAWS was used to simulate the crude oil. A slab with dimensions of 19.859002 Å × 19.859002 Å × 40.107404 Å was built in an enclosed vacuum layer of 25–40 Å along the C axis with single and combined phytochemical molecules. The adsorption locator was used to optimize the molecular structures using smart algorithm annealing in the COMPASSII force field [64, 65] in a condensed phase [31, 51, 65]. A steady energy window of 100 kcal/mol and an adsorption distance of 5–15 Å were maintained between the phytochemical and substrate [58].

2.8 | Gravimetric Analysis

Gravimetric (WL) analysis is commonly used for corrosion monitoring because of its accuracy, simplicity, low cost, and ability to identify damage mechanisms [3, 14, 66]. Unexposed API 5L X65 strip coupons were weighed twice using a Mettler Toledo analytical balance, and the average was calculated to minimize error and ensure reproducibility. The coupons were immersed in 100 mL of 0.5 M HCl test solution; both control and 20, 40, and 60 ppm of GT 8 were then placed in a temperature-controlled water bath for 2, 18, and 24 h at 303, 314, and 328 K, respectively. After exposure, coupons were retrieved, washed with double-distilled water, cleaned with ethanol and acetone, air-dried, weighed twice in a parallel orientation, and averaged for WL calculations. Equations (1)–(4) were used to calculate the corrosion rate, IE, and surface coverage. Here, W_o is the WL without inhibitor, W_i is the WL with inhibitor, CR_o is the uninhibited corrosion rate, CR_i is the inhibited corrosion rate, A is the exposed area in cm^2, t is the exposure time in hours, CR is the general corrosion rate in g/hr/cm^2, and Θ is the surface protection.

$$CR\left(gcm^{-2}hr^{-1}\right) = \frac{W}{A*t}, \tag{1}$$

$$IE_{wl}(\%) = \frac{(W_o - W_i)*100}{W_o}, \tag{2}$$

$$IE_{CR}(\%) = \frac{(CR_o - CR_i)*100}{CR_o}, \tag{3}$$

$$\Theta = \frac{(CR_o - CR_i)}{CR_o}. \tag{4}$$

2.9 | Electrochemical Measurements

Electrochemical measurements were used to assess the effectiveness of the corrosion inhibitor (GT 85) and to gain insight into the corrosion mechanisms, inhibitor type, surface characteristics, electrode kinetics, and stability of the inhibitor film. EIS and PDP

analyses were performed using a Gamry REF 600-24086 potentiostat managed by Gamry Echem Analyst 2 software at 298 K. The experimental setup comprised a three-electrode corrosion cell: a reference electrode (Ag/AgCl with 3 M KCl), graphite counter electrode (8 × 40 mm), and working electrode (API 5L X65 steel coupon, 1 cm^2 surface area). The electrodes were arranged in an open glass cell and connected to a potentiostat via alligator clips.

Prior to EIS and PDP measurements, the working electrode was immersed in 0.5 M HCl for 24 h, with and without the GT 85 inhibitor. The open-circuit potential (OCP) was monitored for 400 s to reach equilibrium before further electrochemical analysis. An alternating current stimulus of 10 mV was applied at frequencies ranging from 0.1 Hz to 100 kHz. The output of the EIS was fitted with equivalent electrical circuits using Gamry Echem Analyst 2 software. The results were the solution resistance (Rs), charge transfer resistance (Rct), double-layer capacitance (Cdl), constant phase element (CPE), magnitude (Y0), and fmax (frequency at which the maximum imaginary impedance ($-Z_{max}$) occurred). The parameter n represents the phase shift (exponent), which indicates surface irregularities and varied from 0.5 1.0. CPE was used to model the double-layer capacitance behavior. Equation (5) relates the pure double-layer capacitance (Cdl) to the charge-transfer resistance and fmax. The corrosion rate (mmpy) was calculated using the equivalent weight (27.92), current density (Icorr), and density (7.870 g/cm^3) of the steel (Equation (6)). The IE, based on the charge transfer resistance with inhibition (Rctin) and without inhibition (Rctun), is given by equation (7). The surface coverage is given by (8).

PDP (Tafel) measurements were conducted at a scan rate of 0.1667 mV/s, with a potential window of −0.25 to +1.25 V relative to OCP. The polarization resistance (R_P) was calculated using the Stern–Geary equation, with βa and βc representing the anodic and cathodic slopes, respectively (equation (10)) The inhibitor efficiency of PDP based on the corrosion current density and polarization resistance (R) for the uninhibited and inhibited corrosion current density (i^{o}_{Corr}, i^{i}_{Corr}) and inhibited (R_i) and uninhibited (R_o) polarization resistance was determined using equations (9) and (12).

$$C_{dl} = \frac{1}{2\pi f_{max}} R_{ct}, \tag{5}$$

$$CR\left(mmy^{-1}\right) = \frac{3270 * EW * ICORR_{den}}{d_{steel}}, \tag{6}$$

$$IE_{EIS}(\%) = \frac{\left(R_{ctin} - R_{ctun}\right)}{R_{ctin}} * 100, \tag{7}$$

$$\text{Surface coverage}(\Theta) = \frac{\left(R_{ctin} - R_{ctun}\right)}{R_{ctin}}, \tag{8}$$

$$IE_{Corr}(\%) = \frac{\left(i^{o}_{Corr} - i_{Corr}\right) * 100}{i^{o}_{Corr}}, \tag{9}$$

$$R_P = \frac{\beta_a \beta_c}{2.30 i^{o}_{Corr}\left(\beta_a + \beta_c\right)}, \tag{10}$$

$$CR_{mmpy} = \frac{3270 * EW * I_{corr}}{d}, \tag{11}$$

$$IE_{RP}(\%) = \frac{\left(R_i - R_0\right)}{R_i} * 100. \tag{12}$$

2.10 | Surface Morphological Analysis

Surface investigations were performed using a SIGMA 300VP field emission scanning electron microscope with EDX, manufactured by Carl Zeiss AG, Germany, to examine the morphology of API 5L X65 steel specimens and the adsorption of GT 85 on the substrate surface after immersion in 0.5 M HCl for 24 h at 303 K, both without and with GT 85 (40 and 60 ppm). EDX was used to analyze the elemental composition of the adsorbed GT 85 and the corrosive species on the steel. The specimens included a baseline, a blank (control) at 303 K in 0.5 M HCl, and samples with 40 and 60 ppm GT 85.

3 | Results and Discussion

3.1 | Analysis of QCP to Establish Phytochemical Synergistic Interaction

3.1.1 | Synergistic Interaction Based on QCP Analysis

The molecular electrostatic potentials (MEPs) shown in Figures 2(a), 2(b), 2(c), 2(d), 2(e), 2(f), 2(g), 2(h), and 2(i) indicate gray, white, red, and flax colors that depict atoms of carbon, hydrogen, oxygen, and silicon. The electron density difference is shown by the red, yellow, green, and blue isosurfaces. The MEP reveals the electrostatic distribution of negative and positive potentials for the different phytochemicals in varying degrees, with the order of intensity, shape, and extent of both positive and negative potentials increasing from red < orange < yellow < green < blue (Figures 2(a), 2(b), 2(c), 2(d), 2(e), 2(f), 2(g), 2(h), and 2(i)). The red regions indicate a high likelihood of covalent bond formation with the vacant d-orbital of iron, and the blue area indicates the electron-receiving potential of iron. The MEP revealed the likelihood of phytochemicals exhibiting electrophilic and nucleophilic attack, leading to synergistic effects when they are combined. The energy gaps of the eight phytochemicals shown in Table 1 and Figures 3(a), 3(b), 3(c), 3(d), 3(e), 3(f), 3(g), 3(h), and 3(i) are greater than 4 eV, which indicates stable adsorption of the phytochemicals on the surface of steel [67]. The energy gap of 9-eicosene is less than 1 (0.08 eV) and its HOMO is −4.95 eV, which suggests that 9-eicosene molecule would be very reactive and be easily adsorbed on steel by donating electron to the empty d-orbital of iron and contribute principally to synergistic interaction [1, 68, 69]. Based on the energy gap, all the phytochemicals are likely to form stable adsorption on the surface of iron, and there will be reinforcement of the adsorption intensity.

The chemical potentials of all nine phytochemicals were negative (Table 1). A negative chemical potential indicates that the phytochemical molecule is reactive and highly likely to donate electrons to the empty d-orbitals of Fe [70]. These nine phytochemicals have a net negative chemical potential and are highly likely to be adsorbed on steel via electron donation and acceptance, leading to the formation of

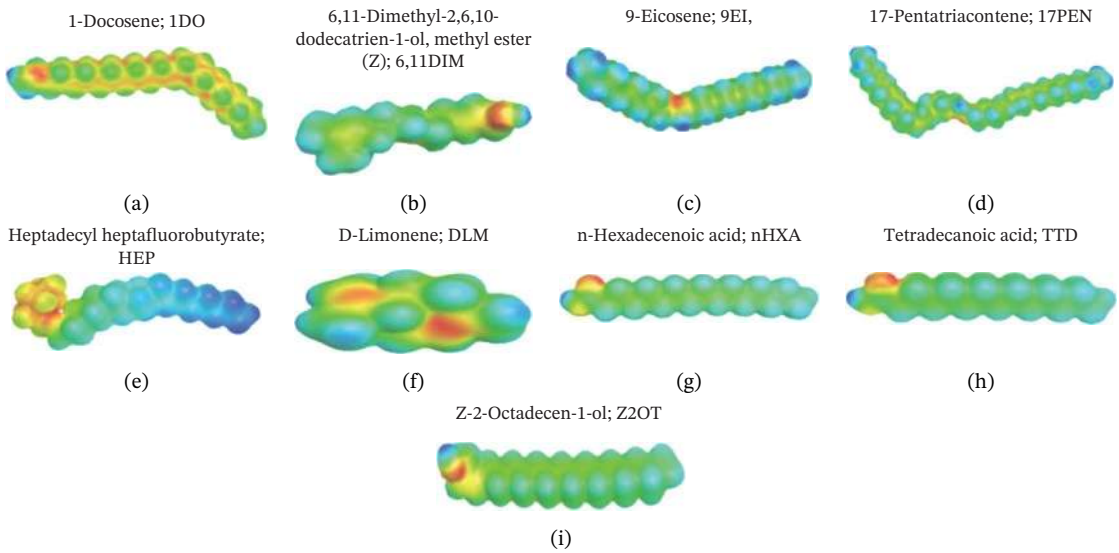


FIGURE 2 | (a–i) Nine (9) phytochemical electrostatic potentials. Basis used was WebMO/MOPAC/Molecular Orbitals/AM1/Singlet.

TABLE 1 | Calculated QCP values for nine phytochemicals.

Quantum chemical parameters (QCPs)	1DO (a)	6, 11 DIM (b)	9EI (c)	17PEN (d)	HEP (e)	DLM (f)	nHXA (g)	TTD (h)	Z2OT (i)
E_{LUMO} (eV)	−0.53	−0.76	−4.85	−0.60	−1.83	−0.56	−0.60	−0.50	−0.61
E_{HOMO} (eV)	−6.55	−5.80	−4.93	−7.21	−7.65	−5.92	−7.21	−7.21	−6.32
Energy gap (eV)	6.02	5.04	0.08	6.60	5.82	5.35	6.60	6.71	5.71
Chemical potential (μ)	−3.54	−3.28	−4.89	−3.91	−4.74	−3.24	−3.91	−3.85	−3.46
Hardness (η) (eV)	3.01	2.52	0.04	3.30	2.91	2.68	3.30	3.36	2.86
Softness (S) (eV^{-1}) (eV)	0.33	0.40	24.39	0.30	0.34	0.37	0.30	0.30	0.35
Back-donation (ΔE) (eV)	−0.75	−0.63	−0.01	−0.83	−0.73	−0.67	−0.83	−0.84	−0.71
Dipole moment (Debye)	0.212	1.69	0.11	0.28	2.99	0.26	1.51	1.53	1.59
Maximum electron charge (ΔN_{max})	0.59	0.65	59.60	0.59	0.81	0.61	0.59	0.57	0.61
Fraction of Electrons (ΔN)	0.58	0.74	25.77	0.47	0.39	0.70	0.47	0.47	0.62

Note: The dipole moment was determined using the optimized structure and WebMO/MOPAC/Molecular Orbitals/AM1/Singlet.

a phytochemical (adsorbate)–iron complex. It is likely that the synergistic effects of the combined phytochemicals will result in increased adsorption intensity and IE. The global softness of 9-eicosene is 24.39 eV^{-1}, and its hardness is 0.04 eV^{-1}. According to the literature, if the global softness value is greater than 5 eV^{-1} and the global hardness value is less than 2 eV, the molecule is highly reactive [71]. The other eight (8) phytochemicals, viz., 1-docosene, 6,11-dimethyl-2,6,10-dodecatrien-1-ol, 17-pentatriacontene, heptadecyl heptafluorobutyrate, D-limonene, hexadecenoic acid, tetradecanoic acid, and Z-2-octadecen-1-ol, have global softness of less than 2 eV^{-1} and hardness that varies between 2.5 and 3.5 eV. A global softness of less than 2 eV^{-1} indicates that the molecule is less reactive, whereas a global hardness of 2–5 eV indicates a moderately reactive molecule [71, 72]. Hence, based on the global hardness parameters, 9-eicosene is the major contributor to the synergistic effects of the nine combined phytochemicals and could be a driver for strengthening the adsorption intensity and IE.

The back-donation of each of the nine (9) phytochemicals was less than zero, and their hardness was greater than zero; hence, electron donation from these phytochemicals to iron is favored according to Gómez et al. [30]. When phytochemicals are combined, there is a high likelihood that back-donation from the nine phytochemicals to the empty d-orbital is enhanced, leading to synergistic effects and increased IE.

Based on studies [72, 73], dipole moment from plant-based phytochemical greater than "1.5(D)" suggests greater ability of the molecule to interact with steel considering other factors like their molecular structure, electronic conjugation, and environmental factors (temperature, pH, and presence of other ions or molecules) [72, 73]. The dipole moment of the five (5) phytochemicals, namely, 6,11-dimethyl-2,6,10-dodecatrien-1-ol, heptadecyl heptafluorobutyrate, n-hexadecenoic acid, tetradecanoic acid, and Z-2-octadecen-1-ol, is greater than 1.5 (D) [72, 73]; this indicates greater ability of these molecules to interact with iron, leading to synergistic effects. Four (4) phytochemicals,

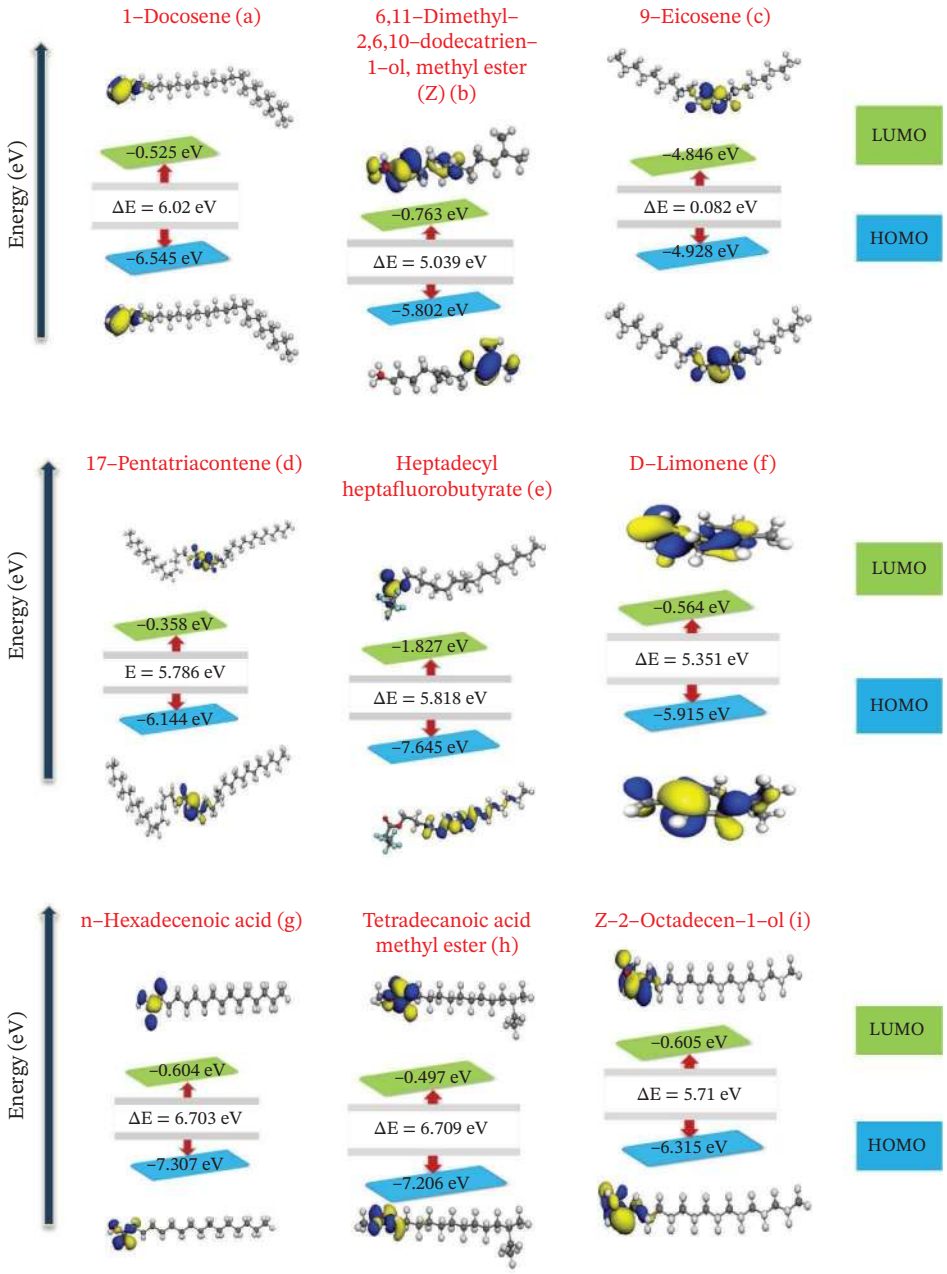


FIGURE 3 | (a–i) Optimized HOMO and LUMO surfaces and energy gaps.

1-docosene, 9-eicosene, 17-pentatriacontene, and D-limonene, have dipole moments less than 1.5, indicating moderate interaction ability [72, 73]. Eight (8) phytochemical molecules, namely, 1-docosene, 6,11-dimethyl-2,6,10-dodecatrien-1-ol, 17-pentatriacontene, heptadecyl heptafluorobutyrate, D-limonene, hexadecenoic acid, tetradecanoic acid, and Z-2-octadecen-1-ol, have maximum electron charge transfer (ΔN_{max}) values between 0.5 and 0.8 (Table 1). This range of values indicates an intermediate reactivity of the eight (8) molecules with the steel surface. ΔN_{max} of 9-eicosene is greater than 1, indicating that the molecule is highly reactive and contributes significantly to synergistic interactions, reinforcing the adsorption of phytochemicals on the surface of steel. According to previous studies [69, 73], if the fraction of electrons (ΔN) is > 0, electron donation from the molecule to the steel surface is favored [74], and if $\Delta N < 0$, electron acceptance by the molecule from the steel surface is favored. A global softness of less than 2 eV^{-1} indicates that the molecule is less reactive, and a global hardness of 2–5 eV^{-1} indicates a moderately reactive molecule [71]. Hence, based on QCP parameters, 9-eicosene is the major contributor to the synergistic effects of the nine combined phytochemicals and is a driver for strengthening the adsorption intensity and IE [52].

3.1.2 | Synergistic Interaction of Phytochemicals Based on OMP

Based on the OMP, 6,11-dimethyl-2,6,10-dodecatrien-1-ol, methyl ester (Z), and D-limonene have a positive, relatively small energy gap between their HOMO and the Fermi level of iron (−5.177 eV) (Table 2). Although their HOMO is at a lower energy level than the Fermi level of iron, they can still donate electrons to iron through thermal or other external factors that promote

electron transfer [69]. Thus, both compounds can donate electrons to the Fe Fermi level, causing a positive shift in their energy levels. In contrast, 9-eicosene's HOMO is at a higher energy level than the iron Fermi level, creating a negative gap, which makes the electron transfer from its HOMO to the Fermi level of iron energetically favorable [1, 48, 75]. Therefore, these three phytochemicals, 6,11-dimethyl-2,6,10-dodecatrien-1-ol, methyl ester (Z), D-limonene, and 9-Eicosene, synergistically interact with steel by donating electrons from their HOMO to the d-orbitals of iron [69].

Additionally, 9-eicosene can accept electrons from the Fermi level of iron by back-donation to its LUMO, due to small positive energy gap between its LUMO and the Fermi level of iron (Table 2) [1, 69, 76, 77]. The combined electron donation from the HOMO of these phytochemicals to the Fermi level of iron and back donation from iron to the LUMO of 9-eicosene create a synergistic interaction that strengthens adsorption on steel [1, 69, 76].

The other phytochemicals, 1-docosene, 17-pentatriacontene, heptadecyl-heptafluorobutyrate, n-hexadecenoic acid, tetradecanoic acid methyl ester, and Z-2-octadecen-1-ol, have a large energy gap between their HOMO and Fermi level of iron, and their HOMO is at a lower energy level. Thus, electron donation from their HOMO to iron's Fermi level is energetically unfavorable [69, 75, 76] (Table 2). Likewise, the Fermi level of iron cannot donate electrons to the LUMO of these compounds because of its large positive energy gap (Table 3), making electron transfer energetically unfavorable [1, 69, 76]. In summary, 6,11-dimethyl-2,6,10-dodecatrien-1-ol, methyl ester (Z), D-limonene, and 9-Eicosene are the key phytochemicals that drive synergistic interactions and reinforce the adsorption intensity on steel, significantly strengthening the bonding of inhibitor agents and enhancing overall performance [1, 69, 76, 77].

3.1.3 | Synergistic Interaction of Phytochemicals Based on Monte Carlo (MC) Simulation Analysis

MC simulations were used to study the adsorption behavior of individual and combined phytochemicals on Fe (111) surfaces in simulated crude oil environments with varying water cuts: 30% (21 H_2O, 9 HCl, 70 LAWS), 50% (41 H_2O, 9 HCl, 50 LAWS), and 70% (61 H_2O, 9 HCl, 30 LAWS). Stable adsorption configurations for both individual and combined phytochemicals at these water cuts were visualized using front and top views (Appendix F and Figure 4). The adsorption energies and energy contribution data for the single and combined phytochemicals are detailed in Appendixes D, E, and F and Figure 5. The individual phytochemical heptadecyl heptafluorobutyrate exhibited the highest and most stable adsorption energies at 30%, 50%, and 70% water cuts, with values of −4431.73, −4968.95, and −5448.18 kcal/mol, respectively. These findings demonstrate the spontaneous exothermic adsorption onto steel surfaces, primarily via σ and π bonds and heteroatoms. Functional groups, heteroatoms, low electronegativity, and high polarizability contribute to low-energy adsorption [15, 16, 51, 66, 78]. Both the van der Waals and electrostatic forces play a role in the adsorption process.

The synergistic effects of the nine combined phytochemicals were assessed at a 30% water cut, revealing a maximum adsorption energy of −4472.22 kcal/mol and a total energy of 6314.03 kcal/mol. This is comparable to the average adsorption energy of individual phytochemicals (−4471.46 kcal/mol) at the same water cut. The combined phytochemicals displaced water and hydrochloric acid, covering a large substrate area and adsorbing parallel to the surface of Fe (111). The synergistic interaction blocked the corrosion sites more effectively than individual adsorption. The simulation results align with QCPs and OMP analyses, showing enhanced adsorption intensity through donor–acceptor interactions.

3.2 | Impact of GT 85

3.2.1 | Gravimetric Measurements

The investigation of the effect of temperature and exposure time on corrosion rates (Tables 4, 5, and 6 and Appendix H Figures A1(a), A1(b), A1(c), A1(d), A1(e), A1(f), A1(g), A1(h), and A1(i) revealed that at 2 h, rates slightly decreased at 328 K for all GT 85 concentrations (Figure A1(a)). After 18 h, the rates dropped sharply at 314 K but generally increased at 328 K for all GT 85 concentrations (Figure A1(b)). At 24 h (Figure A1(c)), the blank rate rose to 4.02×10^{-3} g/cm^{2}h at 328 K but decreased to 2.70×10^{-4} g/cm^{2}h and 2.27×10^{-4} g/cm^{2}h at 20 and 40 ppm of GT 85, respectively. At 303 K (Figure A1(d)), the rates consistently decreased over 24 h for all concentrations. At 314 K (Figure A1(e)), the blank rate dropped from 7.94×10^{-4} to 2.85×10^{-4} g/cm^{2}h over time, with similar declines observed for all inhibitor concentrations. At 328 K (Figure A1(f)), 20 and 40 ppm showed decreasing rates, but the blank and 60 ppm showed increasing rates. After 18 and 24 h at higher temperatures, GT 85 desorption reduced the effectiveness, causing higher corrosion rates. Despite this, GT 85 remained stable and effective up to 328 K, achieving maximum inhibitor efficiencies of 72% at 303 K, 88% at 314 K, and 94% at 328 K at 60 ppm after 24 h (Table 6 and Figures A1(g), A1(h), and A1(i)). These findings indicate that GT 85's phytochemicals' synergistic effects are mainly responsible for corrosion inhibition and are effective at low concentrations and thermally stable up to 328 K.

3.2.2 | Adsorption Studies

The adsorption isotherm describes how GT 85 binds to API 5L X65 steel to reduce acidic corrosion, evaluated at 303, 314, and 328 K and exposure times of 2, 18, and 24 h. Three models—Langmuir, Freundlich, and Temkin—were applied to the experimental data to identify the most accurate representation of the adsorption process. Equations (13)–(15)) define these models using parameters Θ (surface coverage), K_{ads} (adsorption equilibrium constant), and C_{inh} (inhibitor concentration).

$$\text{Langmuir: } \frac{C_{inh}}{\Theta} = \frac{1}{K_{ads}} + C_{inh}, \tag{13}$$

$$\text{Freundlich: } \log\Theta = n\log C_{inh} + \log K_{ads}, \tag{14}$$

$$\text{Temkin: } \Theta = -\frac{1}{2}a\ln K_{ads} - \frac{1}{2}a\ln C_{inh}. \tag{15}$$

The adsorption data were best described by the Langmuir and Freundlich isotherms, with high regression coefficients ($R^2 = 0.99996$ and 0.97856, respectively) for 24 h exposure at 328 K (Figure 6 and Table 7). The Langmuir adsorption equilibrium constants (K_{ads}) were determined using the reciprocal of the intercepts of the linear plots, whereas the Freundlich

TABLE 2 | Orbital matching based on HOMO and Fermi energy level.

Phytochemical molecule	EHOMO (eV)	ΔE between HOMO and Fermi level of iron (−5.177 eV) [69]	Interpretation of results
1-Docosene	−6.545	1.368	Positive and large HOMO is at a lower energy level than the iron Fermi level (−5.177 eV) Electron transfer from HOMO to iron the Fermi level is energetically unfavorable
17-Pentatriacontene	−7.206	2.029	
Heptadecyl heptafluorobutyrate	−7.645	2.468	
n-Hexadecenoic acid	−7.206	2.029	
Tetradecanoic acid methyl ester	−7.206	2.029	
Z-2-Octadecen-1-ol	−6.315	1.138	
6,11-Dimethyl-2,6,10-dodecatrien-1-ol, methyl ester (Z)	−5.802	0.625	Positive and relatively small HOMO at lower energy level than the iron Fermi level (−5.177 eV) but can still donate an electron to the iron Fermi level, by thermal energy or other external factors
D-Limonene	−5.915	0.738	
9-Eicosene	−4.928	−0.249	Negative HOMO at higher energy level than the iron Fermi level (−5.177 eV). Electron transfer from HOMO to iron Fermi level is energetically favorable

TABLE 3 | Orbital matching based on LUMO and Fermi energy level.

Phytochemical molecule	ELUMO (eV)	ΔE between Fermi level of iron (−5.177 eV) and LUMO	Interpretation of results
1-Docosene	−0.525	4.652	
6,11-Dimethyl-2,6,10-dodecatrien-1-ol, methyl ester (Z)	−0.763	4.414	
17-Pentatriacontene	−0.604	4.573	Positive and large Electron transfer from Iron Fermi level to LUMO is energetically unfavorable
Heptadecyl heptafluorobutyrate	−1.827	3.350	
D-Limonene	−0.564	4.613	
n-Hexadecenoic acid	−0.604	4.573	
Tetradecanoic acid methyl ester	−0.497	4.680	
Z-2-Octadecen-1-ol	−0.605	4.572	
9-Eicosene	−4.846	0.331	Positive and small Electron transfer from Iron Fermi level to LUMO is energetically favorable LUMO is in a suitable position to accept electrons

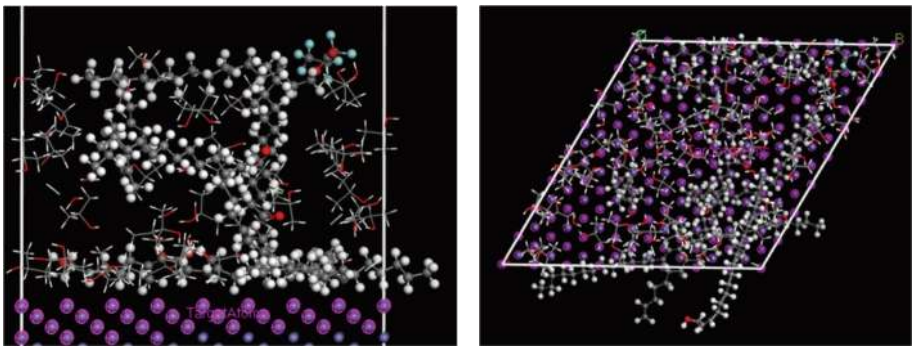
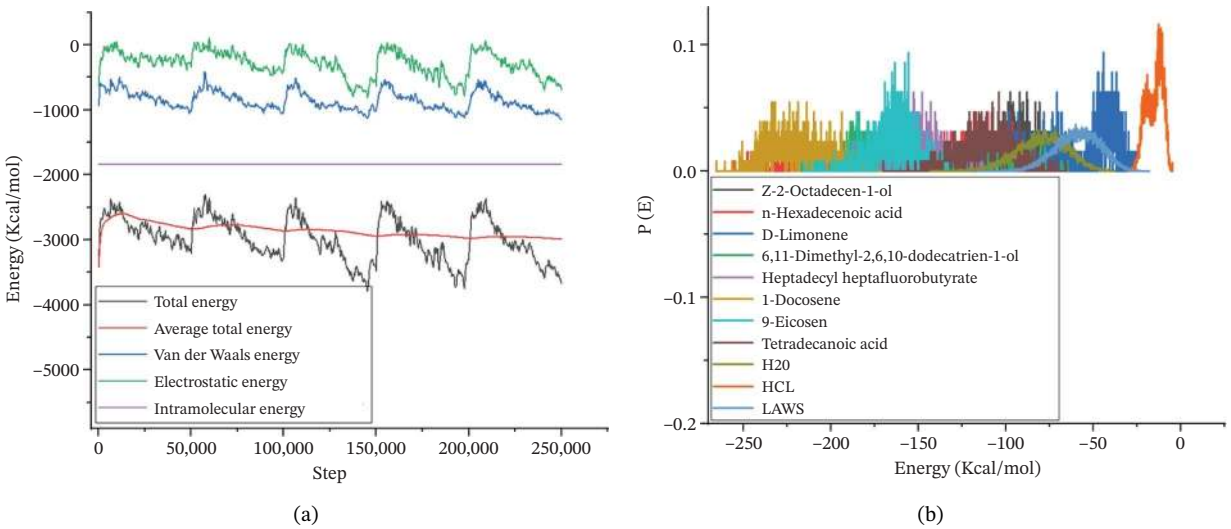


FIGURE 4 | Front and top views of the stable adsorption configuration for the combined phytochemicals/Fe (111) interface with a 30% water cut (21 H_2O, 9 HCl, combined phytochemicals, and 70 LAWS system), as obtained by the adsorption locator module using the compass force field.



(a) (b)

FIGURE 5 | Distribution of adsorption energy and the contribution of various energy forms during Monte Carlo (MC) calculations for nine combined phytochemicals. (a) Contribution of the different energy types during the MC calculations for combined phytochemical on iron (Fe). (b) Distribution of the adsorption energies for combined phytochemical on the iron (Fe).

TABLE 4 | General corrosion rates and inhibition efficiency of API 5L X65 steel at various immersion times in a 0.5 M HCl solution with different concentrations of GT 85 (303 K).

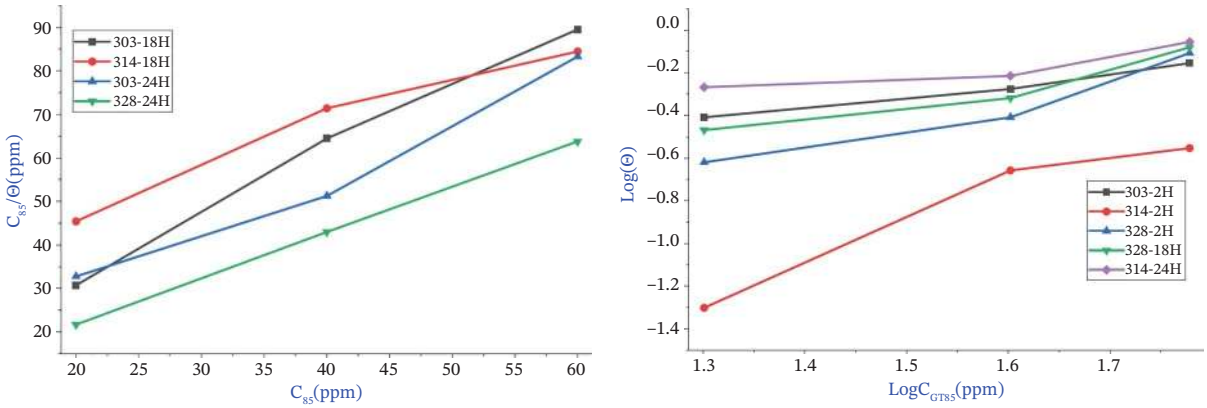
Immersion time (h)	GT 85 (ppm)	WLm (g)	Corrosion rate (g/cm^2h)	θ	IE_{CR} (%)	IE_{WL} (%)
2	Blank	3.35E − 02 ± 9.50E − 03	1.19E − 03 ± 3.37E − 04			
2	20	2.04E − 02 ± 4.30E − 03	7.23E − 04 ± 1.52E − 04	0.39	39	39
2	40	1.57E − 02 ± 4.00E − 03	5.57E − 04 ± 1.42E − 04	0.53	53	53
2	60	9.95E − 03 ± 1.95E − 03	3.53E − 04 ± 6.9E − 05	0.70	70	70
18	Blank	1.84E − 01 ± 1.26E − 01	7.24E − 04 ± 4.98E − 04			
18	20	6.51E − 02 ± 3.80E − 02	2.57E − 04 ± 1.50E − 04	0.65	65	65
18	40	7.03E − 02 ± 4.00E − 02	2.77E − 04 ± 1.58E − 04	0.62	62	62
18	60	6.02E − 02 ± 2.81E − 02	2.37E − 04 ± 1.11E − 04	0.67	67	67
24	Blank	1.21E − 01 ± 5.30E − 02	3.57E − 04 ± 1.56E − 04			
24	20	4.67E − 02 ± 2.57E − 02	1.38E − 04 ± 7.59E − 05	0.61	61	61
24	40	2.60E − 02 ± 1.52E − 02	7.68E − 05 ± 4.49E − 05	0.78	78	78
24	60	3.43E − 02 ± 1.25E − 02	1.01E − 04 ± 3.71E − 05	0.72	72	72

TABLE 5 | General corrosion rates and inhibition efficiency (IE) of API 5L X65 steel at various immersion times in 0.5 M HCl solution with different concentrations of GT 85 (314 K).

Immersion time (h)	GT 85 (ppm)	WL (g)	Corrosion rate (g/cm^2h)	θ	EI (%)	IE (%)
2	Blank	2.31E − 02 ± 1.50E − 04	7.98E − 04 ± 5.17E − 06			
2	20	2.20E − 02 ± 2.00E − 04	7.59E − 04 ± 6.90E − 06	0.05	5	5
2	40	1.81E − 02 ± 6.24E − 04	6.24E − 04 ± 3.45E − 06	0.22	22	22
2	60	1.66E − 02 ± 5.72E − 04	5.72E − 04 ± 3.45E − 06	0.28	28	28
18	Blank	4.97E − 02 ± 1.91E − 04	1.91E − 04 ± 9.58E − 07			
18	20	2.80E − 02 ± 6.50E − 04	1.07E − 04 ± 2.49E − 06	0.44	44	44
18	40	2.18E − 02 ± 2.50E − 04	8.33E − 05 ± 9.58E − 07	0.56	56	56
18	60	1.47E − 02 ± 5.50E − 04	5.61E − 05 ± 2.11E − 06	0.71	71	71
24	Blank	9.91E − 02 ± 6.50E − 04	2.85E − 04 ± 1.87E − 06			
24	20	4.60E − 02 ± 2.50E − 04	1.32E − 04 ± 7.18E − 07	0.54	54	54
24	40	3.82E − 02 ± 3.00E − 04	1.10E − 04 ± 8.62E − 07	0.61	61	61
24	60	1.18E − 02 ± 9.95E − 02	3.38E − 05 ± 2.86E − 04	0.88	88	88

TABLE 6 | General corrosion rates and inhibition efficiency (IE) of API 5L X65 steel at various immersion times in 0.5 M HCl solution with different concentrations of GT 85 (328 K).

Immersion time (h)	GT 85 (ppm)	WLm (g)	Corrosion rate (g/cm^2h)	θ	IE (WL)	IE (CR)
2	Blank	2.46E − 02 ± 0	7.94E − 04 ± 0			
2	20	1.88E − 02 ± 6.00E − 04	6.06E − 04 ± 1.94E − 05	0.24	24	24
2	40	1.50E − 02 ± 3.50E − 04	4.82E − 04 ±.13E − 05	0.39	39	39
2	60	5.45E − 03 ± 3.50E − 04	1.76E − 04 ± 1.13E − 05	0.78	78	78
18	Blank	3.28E − 01 ± 4.50E − 04	1.18E − 03 ± 0			
18	20	2.16E − 01 ± 1.50E − 04	7.76E − 04 ± 5.38E − 07	0.34	34	34
18	40	1.72E − 01 ± 1.50E − 04	6.16E − 04 ± 5.38E − 07	0.48	48	48
18	60	5.49E − 02 ± 2.50E − 04	1.97E − 04 ± 8.96E − 07	0.83	83	83
24	Blank	1.50E+00 ± 1.23E+00	4.02E − 03 ± 3.30E − 03			
24	20	1.19E − 01 ± 1.16E − 01	3.19E − 04 ± 3.12E − 04	0.92	92	92
24	40	1.01E − 01 ± 3.00E − 04	2.70E − 04 ± 8.06E − 07	0.93	93	93
24	60	8.46E − 02 ± 0	2.27E − 04 ± 4.80E − 18	0.94	94	94



(a) (b)

FIGURE 6 | Fitting of adsorption isotherms of GT 85 over API 5L X65 steel in 0.5 M HCl. (a) Langmuir adsorption isotherms at 303, 314, and 328 K for 2, 18, and 24 h. (b) Freundlich adsorption isotherms at 303, 314, and 328 K for 2 and 18 h.

constants were calculated as the antilogarithm of the intercepts. Both models explain GT 85 adsorption on API 5L X65 steel at different temperatures and exposure times. Equation (16) was used to correlate the adsorption equilibrium constant (K_{ads}) with the standard free energy of adsorption (ΔG_{ads}) [79]. Here, T is the temperature of water in Kelvin (298 K), R is the universal gas constant, and the solvent concentration was taken as 55.5 mol/L. The value of K_{ads} decreased slightly at 314 K and increased at 328 K for 2, 18, and 24 h, indicating stronger adsorption at higher temperatures. The ΔG_{ads} values (ranging from −1.68 to −10.45 kJ/mol) for all conditions confirm that the process is mainly physical adsorption (physisorption), with increased adsorption efficiency and reduced desorption as temperature increases [47, 80].

$$\Delta G_{ads} = -RT\ln\left(55.5K_{ads}\right). \tag{16}$$

3.2.3 | EIS

The Nyquist plots obtained are semicircles which indicate inductive loops [81] (Figure 7(a)). The Nyquist plots suggest that the corrosion of API 5L X65 steel in 0.5 M HCl solution was due to charge transfer [1, 3, 14]. As the concentration of GT 85 increased, the size of the semicircle plots increased. This is attributed to the increased adsorption and surface protection of API 5L X65 steel [82, 83]. The EIS data were fitted to an equivalent circuit (Figure 7(a)) consisting of the charge-transfer resistance (R_{ct}) connected in a parallel electrical circuit with a CPE in series with the solution resistance (R_s). The interception of the capacitive loop at high frequencies indicates the solution resistance (R_s), and at low frequencies, it indicates the charge transfer plus the solution resistance ($R_{ct} + R_s$). The results indicate that there is an increase in the charge transfer resistance (2.401 to 46.103 Ω cm^2) and IE with an increase in GT 85 concentration (10%–60%). These results further suggest the adsorption of phytochemicals on API 5L X65 steel and the displacement of corrosive species with a positive shift in the OCP (Figure 8(a)). This pattern can be attributed to the combined synergistic effects of the nine phytochemicals. The combined synergistic effects resulted in the formation of a thicker surface film with increased protection coverage area. These results support the MC results discussed previously. The inherent limitations of Nyquist plots, such as their inability to reveal the exact frequencies at which impedance is measured, are overcome by Bode phase angle plots (Figure 7(b)) and Bode modulus or impedance magnitude plots (Figure 7(c)). These plots show the exact frequencies of the phase angle and the impedance of the corrosion system. The plots (Figures 7(b) and 7(c)) show that in the absence and presence of GT 85 at different inhibitor concentrations, the impedance modulus and phase angles increased to a maximum with increasing GT 85 concentration. This increase is profound at low frequencies (Bode plots), which implies higher inhibition and formation of a protective film (layer) acting as a barrier to corrosive species ingress [81]. The reduction in the double-layer capacitance (C_{dl}) from 128.412 μF cm^{-2} (blank) to 41.228 μF cm^2 at 60 ppm and CPE amplitude confirmed the formation of a protective layer of GT 85 and the displacement of water molecules based on the Helmholtz model [81] (Table 8 and Figure 8(b)). EIS and gravimetric analyses indicate that GT 85 has the capacity to reduce the local dielectric constant while increasing the electrical double-layer thickness of the GT 85 film. The slight variation in CPE exponents further confirms that corrosion is caused by an activation-controlled mechanism [84, 85]. The stable charge transfer resistance suggests that GT 85 has good persistence and can be deployed to control API 5L X65 steel acid corrosion. These results suggest that the combined phytochemicals are the active ingredients responsible for corrosion inhibition and synergistic effects exhibited by GT 85.

3.2.4 | PDP

Table 9 and Figure 7(d) show that adding GT 85 at concentrations between 20 and 40 ppm increased both the anodic and cathodic segments. Increasing the GT 85 concentration lowered the current densities, which reduced both anodic dissolution and cathodic hydrogen evolution. The corrosion rate decreased significantly from 115.41 to 0.00772 mmpy, confirming the synergistic effect of the combined phytochemicals and supporting QCP, OMP, and MC simulation analyses. The Tafel plots indicate that GT 85 acts as an anodic inhibitor, as the E_{corr} displacement between the uninhibited and highest-inhibited samples at 60 ppm exceeds 85 mV. The maximum IE was 99.9% for both the

TABLE 7 | Thermodynamic adsorption of GT 85 at 303, 314, and 328 K and 2, 18, and 24 h.

Model	Time (h)	Temperature (K)	GT 85 (ppm)	R^2	Intercept	Slope	K_{ads}	ΔG_{ads} (kJ mol^{-1})
Freundlich	2	303	20, 40.60	9.85E − 01	−1.10E + 00	5.23E − 01	3.34E − 01	−7.2365
Freundlich	2	314	20, 40.60	9.42E − 01	−3.38E + 00	1.63E + 00	3.41E − 02	−1.5773
Freundlich	2	328	20, 40.60	9.38E + 00	−1.99E + 00	1.93E + 00	1.37E − 01	−5.0195
Langmuir	18	303	20, 40.60	9.93E − 01	2.83E + 00	2.94E + 01	3.49E − 01	−7.3443
Langmuir	18	314	20, 40.60	9.65E − 01	2.81E + 01	1.95E + 01	3.56E − 02	−1.6837
Freundlich	18	328	20, 40.60	9.23E − 01	−1.50E + 00	7.78E − 01	2.22E − 01	−6.2243
Langmuir	24	303	20, 40.60	9.77E − 01	5.25E + 00	2.53E + 01	1.89E − 01	−5.8219
Freundlich	24	314	20, 40.60	8.25E − 01	−8.28E − 01	4.16E − 01	4.37E − 01	−7.9000
Langmuir	24	328	20, 40.60	1.00E + 00	7.69E − 01	2.10E + 01	1.22E + 00	−10.452

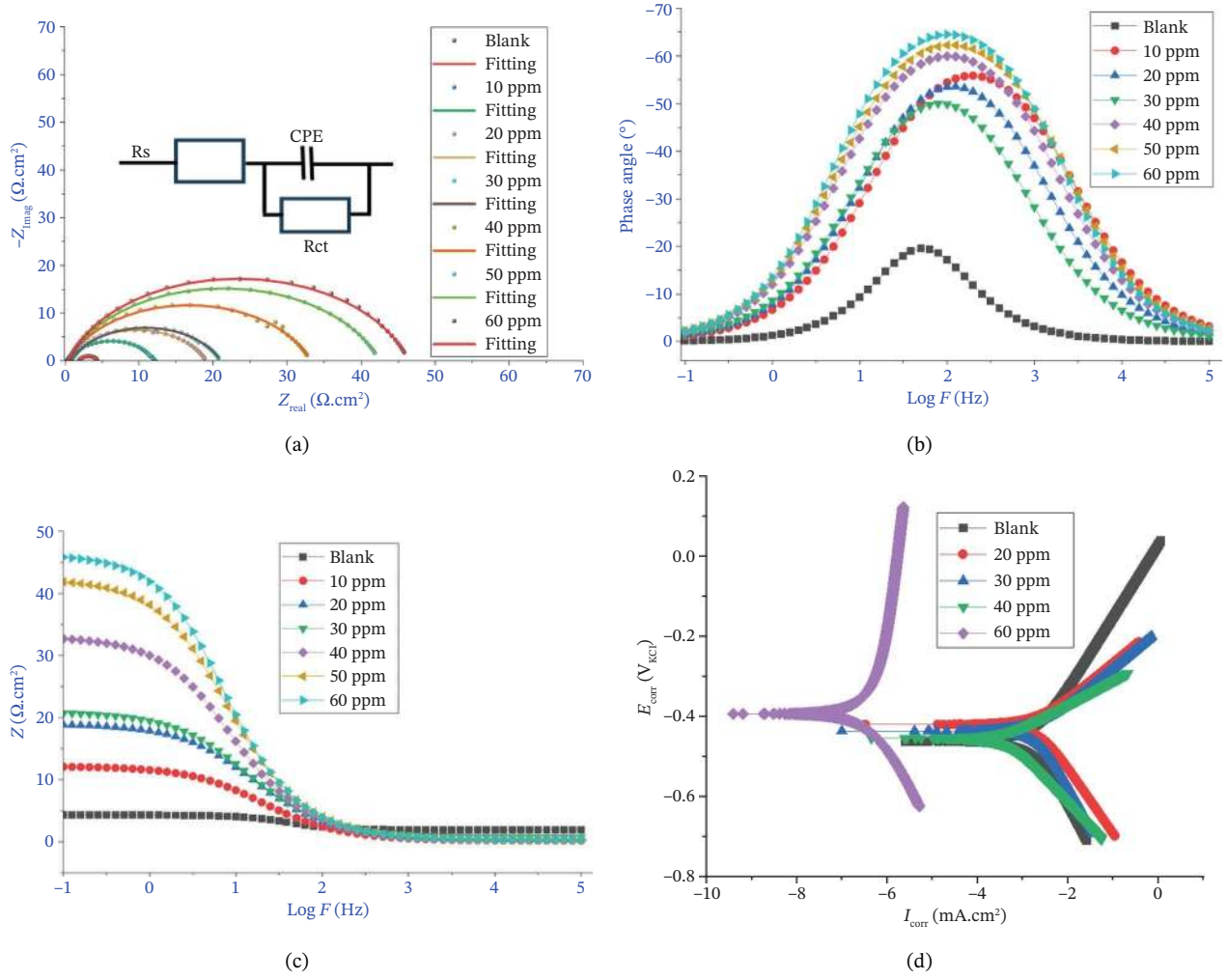
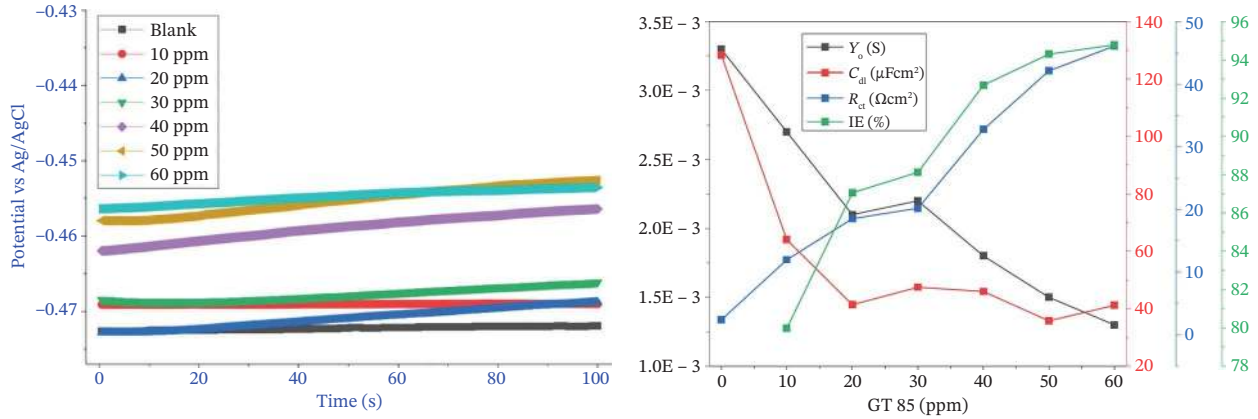


FIGURE 7 | (a) Nyquist plots in the absence and presence of a variable concentration of Greentreat (GT) 85 in 0.5 M HCl with equivalent circuit diagram. (b) Bode phase angle plots. (c) Bode modulus. (d) PDP (Tafel) plots.



(a) (b)

FIGURE 8 | (a) Open-circuit potential (OCP) measurements with time in the absence and presence of a variable concentration of Greentreat (GT) 85 in 0.5 M HCl. (b) EIS plots for Y_o, C_{dl}, R_{ct}, and IE (%) in the absence and presence of a variable concentration of Greentreat (GT) 85 in 0.5 M HCl.

TABLE 8 | Electrochemical impedance spectroscopy characteristics for API 5L X65 carbon steel corrosion in 0.5 M HCl at different concentrations of Greentreat 85.

GT 85 (ppm)	R_s (Ω cm^2)	R_{ct} (Ω cm^2)	n	Y_o S*s^a	C_{dl}(μF cm^{-2})	IE (%)
Blank	1.903 ± 0.012	2.401 ± 0.032	0.904 ± 0.01.6	0.0033 ± 3.06E − 04	128.412	
10	0.207 ± 0.002	11.992 ± 0.085	0.768 ± 0.003	0.0027 ± 6.39E − 5	64.049	79.98 ± 0.120
20	0.474 ± 0.004	18.545 ± 0.139	0.773 ± 0.004	0.0021 ± 5.07E − 5	41.418	87.06 ± 0.072
30	0.748 ± 0.005	20.221 ± 0.161	0.764 ± 0.004	0.0022 ± 5.68E − 5	47.530	88.13 ± 0.0616
40	0.357 ± 0.003	32.798 ± 0.256	0.787 ± 0.003	0.0018 ± 3.47E − 5	46.003	92.68 ± 0.0391
50	0.322 ± 0.003	42.150 ± 0.329	0.795 ± 0.003	0.0015 ± 2.70E − 5	35.796	94.30 ± 0.0304
60	0.322 ± 0.002	46.103 ± 0.357	0.816 ± 0.003	0.0013 ± 2.36E − 5	41.228	94.79 ± 0.0281

corrosion rate and polarization resistance measurements. The average absolute value of the anodic to cathodic Tafel slopes was greater than 1, signifying anodic control of corrosion inhibition by blocking the active anode more effectively than the reduction of oxygen and hydrogen.

Discrepancies in IE values from the WL, EIS, and PDP methods are likely due to differences in coupon area, exposure time, and GT 85 desorption, as well as the distinct measurement approaches of each method. Similar inconsistencies have been reported for crude extracts. Overall, the observed corrosion inhibition behavior is attributed to the synergistic effect of the nine dominant inhibitors, which serve as effective agents for corrosion prevention.

3.2.5 | Surface Analysis

FE-SEM images and EDX analysis of API 5L X65 steel in 0.5 M HCl (baseline, blank, and GT 85-inhibited specimens at 40 and 60 ppm) are shown in Figure 9. The baseline (Figure 9(a)) displays a clean steel surface, with EDX indicating high iron (Fe) and minor alloying elements. The

TABLE 9 | Polarization data of API 5L X65 steel corrosion in 0.5 M HCl with varying concentrations of GT 85.

GT 85 (ppm)	Blank	20	30	40	60
E_{corr} (mv)	−494 ± 3.0	−419 ± 2.5	−436 ± 2.1	−454 ± 2.0	−393 ± 1.5
I_{corr} (mA/cm^2)	9.95 ± 0.2	2.16 ± 0.09	2.16 ± 0.09	0.44 ± 0.03	6.66E-04 ± 1.0E-08
βa (mv/dec)	2.81E + 02	9.22E + 01	9.37E + 01	6.03E + 01	9.71E + 02
βb (mv/dec)	4.34E + 00	1.63E + 02	2.05E + 02	1.20E + 02	2.53E + 02
R_P (Ω)	0.186 ± 0.004	11.88 ± 0.495	12.93 ± 0.538	39.88 ± 2.726	131,051.93 ± 1.97
CR (mmpy)	115.41 ± 2.32	25.05 ± 1.044	25.10 ± 1.044	5.09 ± 3.48E − 01	7.72E-03 ± 1.16E − 07
EI_{CORR} (%)		78.3 ± 4.69E − 03	78.2 ± 4.68E − 03	95.6 ± 2.13E − 03	99.9 ± 0
EI_{PR} (%)		98.42 ± 3.39E − 04	98.6 ± 3.109E − 04	99.53 ± 2.27E − 04	99.9 ± 0

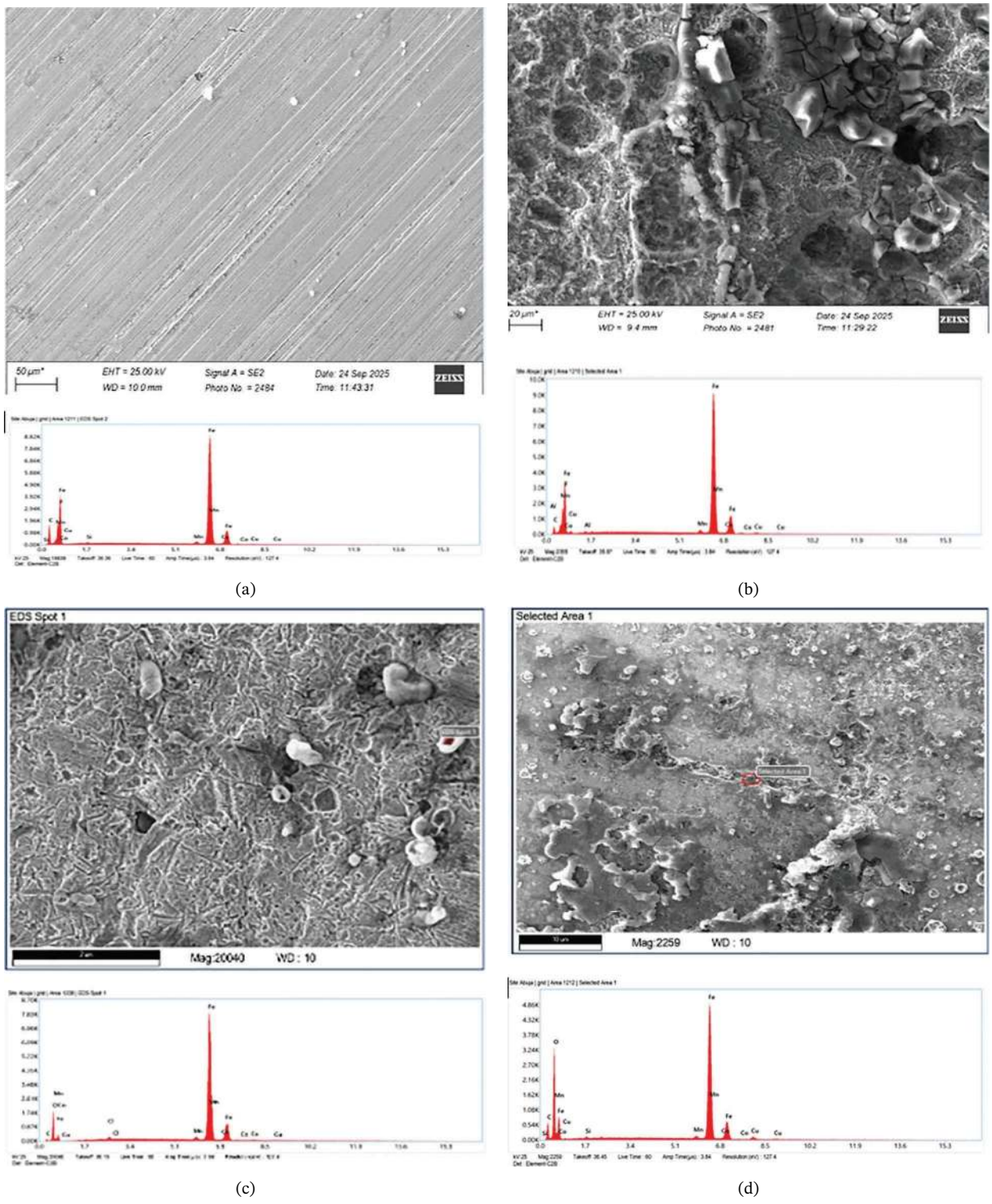


FIGURE 9 | FE-SEM images and EDX analysis diagram of API 5 L X65 high-grade, high-strength low-alloy (HSLA) carbon steel specimen (a) baseline 50 µm clean HSLA surface with EDX; (b) blank 20 µm HSLA immersed in 0.5 M HCl without GT 85 with EDX ; (c) HSLA 2 µm immersed in 0.5 M HCl with 40 ppm GT 85 with EDX; (d) HSLA 10 µm immersed in 0.5 M HCl with 60 ppm GT 85 with EDX.

blank sample (Figure 9(b)) shows pit formation and a strong Fe peak, suggesting Fe dissolution due to the breakdown of the protective film of the steel. At 40 and 60 ppm GT 85 (Figures 9(c) and 9(d)), the inhibitor was uniformly adsorbed, with greater coverage at 60 ppm. EDX at 40 ppm showed Fe and minor Cl, while at 60 ppm, Fe, C, O, and Si were present; the increase in carbon and oxygen (hydroxyl or carbonyl groups) indicated GT 85 adsorption and reduced acidic dissolution (absence of Cl). These results confirm that GT 85 effectively inhibits acid corrosion, consistent with the WL, EIS, and PDP findings, owing to synergistic phytochemical interactions.

4 | Conclusions

The novelty of this study lies in the investigation of the synergistic corrosion interaction of nine unique molecular combinations (phytochemicals), 1-docosene, 6,11-dimethyl-2,6,10-dodecatrien-1-ol methyl ester (Z), 9-eicosene, 17-pentatriacontene, heptadecyl heptafluorobutyrate, D-limonene, n-hexadecenoic acid, tetradecanoic acid, and Z-2-octadecen-1-ol, using an innovative DFT combination of QCP, OMP analysis, and MC simulation in an acidic environment containing 30% water cut in crude oil modeled using a LAWS to accurately predict synergistic behavior. The insight gained from DFT and MC simulations for the nine unique molecules was exploited to develop GT 85 using WL and electrochemical methods (EIS and PDP) and supported by FE-SEM and EDX analyses. The developed product, GT 85, is thermally stable up to 328 K and exhibits high efficiency and persistence. This study offers quantitative evidence that the synergistic interactions of phytochemicals can be accurately predicted for the design of novel high-performance inhibitors for targeted industrial applications. The methods used in this study will open up avenues for further research and product development. The series of results led to the following salient conclusions:

i. GT 85 significantly reduces the acidic corrosion of API 5L X65 steel. WL showed inhibition efficiencies of 72% at 303 K, 88% at 314 K, and 94% at 328 K after 24 h.

ii. QCP analysis showed that all nine phytochemicals enhance synergistic interactions through nucleophilic and electrophilic attacks.

iii. The OMP showed that 6,11-dimethyl-2,6,10-dodecatrien-1-ol methyl ester (Z), D-limonene, and 9-eicosene are the key phytochemicals responsible for enhancing synergistic interaction and adsorption intensity on the Fe surface, while other six phytochemicals improved the stability of the adsorbed film.

iv. MC simulations demonstrated that the nine phytochemicals were spontaneously adsorbed onto the Fe (111) surface, with a significant adsorption energy of −4472.220 kcal/mol in an acidic environment.

v. Nyquist plots exhibited semicircular shapes, indicating inductive loops and an activation-controlled (charge transfer) corrosion mechanism for the API 5L X65 steel in acidic media. The validation of the corrosion mechanism was further supported by slight changes in the CPE exponent. Increasing GT 85 concentration resulted in larger semicircles, suggesting enhanced adsorption and surface protection. EIS results showed that adding GT 85 increased charge transfer resistance (Rct) from 2.401 Ω cm^2 (blank) to 46.103 Ω cm^2 (60 ppm), while double-layer capacitance (Cdl) and the CPE amplitude (Y_0) decreased from 128.412 to 41.228 μF cm^{-2} and 0.0033 S∗s^a (blank) to 0.0013 S∗s^a, respectively. GT 85 demonstrated a high IE of 94.79% and maintained a stable charge transfer resistance, indicating effective and persistent corrosion inhibition at low dosages in acidic environments.

vi. The Tafel plot analysis demonstrated that increasing the dosage of GT 85 led to higher values in both anodic and cathodic segments, while simultaneously decreasing the corrosion current densities, from 9.95 mA/cm^2 to 6.66 E − 04 mA/cm^2. This indicates a reduction in both the anodic dissolution and cathodic hydrogen evolution processes. GT 85 was declared an anodic inhibitor because of a shift in the corrosion potential (E_{corr}) of more than 85 mV in the positive direction between the uninhibited and the most inhibited system (at 60 ppm). Both the corrosion rate and polarization resistance methods yielded a maximum IE of 99.9%. Analysis of the Tafel slopes showed that the ratio of the anodic to cathodic slopes generally exceeded 1, suggesting that the inhibition mechanism was predominantly under anodic control. This means that GT 85 hindered the oxidation of the active anodic sites, outpacing the reduction at the cathodic sites. These results highlight the synergistic effects of the combined phytochemicals in GT 85 and are consistent with QCPs, orbital molecular properties (OMP), and MC simulation analyses.

vii. The adsorption of GT 85 on API 5L X65 steel in 0.5 M HCl aligned well with both Langmuir and Freundlich isotherm models, as their high R^2 values are greater than 0.9 and close to 1. This strong fit with the experimental data suggests that GT 85 adsorption occurs primarily as a monolayer on the steel surface (Langmuir isotherm), with some secondary multilayer adsorption also occurring (Freundlich isotherm).

viii. FE-SEM and EDX analyses showed that corrosion was reduced and a protective GT 85 film was formed on API 5L X65 steel.

x. Multitechnique analysis confirmed that the nine phytochemicals studied work together synergistically to inhibit corrosion in 0.5 M HCl by utilizing their rich active sites, heteroatoms, and interactions such as van der Waals forces and electrostatic attraction with the steel surface.

xi. The unique molecular phytochemical combinations investigated are environmentally friendly alternatives to synthetic chemical inhibitors.

5 | Recommendations

The dominant phytochemicals, 1-docosene, 6,11-dimethyl-2,6,10-dodecatrien-1-ol methyl ester (Z), 17-pentatriacontene, heptadecyl heptafluorobutyrate, D-limonene, n-hexadecenoic acid, tetradecanoic acid methyl ester, Z-2-octadecen-1-ol, and 9-eicosene, can be further isolated to study their anticorrosion properties under static and dynamic flow conditions similar to those obtained in the oil and gas industry.

6 | Implications for Research, Practice, and Society

This study advances our understanding of how plant-based phytochemicals interact with iron surfaces, supporting the development of eco-friendly corrosion inhibitors and promoting green chemistry. GT 85, a novel product, is expected to reduce equipment failures and extend the infrastructure lifespan, which can lower maintenance costs and boost competitiveness. Additionally, GT 85 may decrease environmental pollution, workers' chemical exposure, and the risk of major incidents. By reducing

the costs of corrosion and manufacturing, GT 85 could foster economic growth and support a more sustainable society.

Acknowledgments

The authors are grateful to AUST Abuja for granting access to the African Development Bank's Materials Science and Engineering Laboratory.

Funding

No funding was received for this manuscript.

Disclosure

The authors concur with work submitted and pledge their support to research in this field.

Ethics Statement

This article has not been submitted to any other journal, and the results have never been made public. Plagiarism has been avoided to the best of our abilities.

Consent

The authors have consented to the publication of this manuscript.

Conflicts of Interest

The authors declare no conflicts of interest.

Data Availability Statement

Data will be provided upon request.

References

1. J. I. Emmanuel, F. O. Ngasoh, A. Bello, V. C. Anye, and P. A. Onwualu, "Phytochemical Study of Some Plant Extracts to Assess Their Synergistic Corrosion Inhibition Performance-A Comparative Analysis," *Research Square* (June 2024): https://doi.org/10.21203/rs.3.rs-4498767/v1.

2. C. O. Okoye, F. Odette, A. Bello, J. I. Emmanuel, E. O. Onche, and E. N. Okon, "Metronidazole Mediated Potassium Iodide as High-Performance Deterioration Retardant for Mild Steel in an Acidic Media," *Journal of Dispersion Science and Technology* 46 (May 2024): 1–12, https://doi.org/10.1080/01932691.2024.2348493.

3. I. G. Alberts, J. I. Emmanuel, F. O. Ngasoh, A. Bello, A. P. Onwualu, and V. C. Anye, "Neem Leaf Extract as Corrosion Prevention and Inhibition Agent for Mild Steel in Acid Medium," in *2023 2nd International Conference on Multidisciplinary Engineering and Applied Science (ICMEAS)* (IEEE, November 2023), 1–6, https://doi.org/10.1109/ICMEAS58693.2023.10429861.

4. N. P. Swathi, S. Samshuddin, A. T. Aljohani, et al., "Corrosion Mitigation of Carbon Steel Using Triazole Mannich Base Derivatives: Correlation of Electrochemical Studies With Quantum Chemical Calculations," *Arab Journal of Basic and Applied Sciences* 30, no. 1 (December 2023): 496–512, https://doi.org/10.1080/25765299.2023.2249227.

5. D. Daoud, T. Douadi, H. Hamani, D. Ghobrini, and K. Aiboud, "Experimental and Theoretical Study of a New Synthesized Quinoline Derivative as Greene Inhibitor of Corrosion for the Cooling Circuits in Desalinated Water," in *2015 3rd International Conference on Control, Engineering & Information Technology (CEIT)* (IEEE, May 2015), 1–5, https://doi.org/10.1109/CEIT.2015.7233032.

6. O. Dagdag, A. Berisha, Z. Safi, et al., "DGEBA-Polyaminoamide as Effective Anti-Corrosive Material for 15CDV6 Steel in NaCl Medium: Computational and Experimental Studies," *Journal of Applied Polymer Science* 137, no. 8 (February 2020): 48402, https://doi.org/10.1002/app.48402.

7. B. R. Fazal, T. Becker, B. Kinsella, and K. Lepkova, "A Review of Plant Extracts as Green Corrosion Inhibitors for CO_2 Corrosion of Carbon Steel," *NPJ Materials Degradation* 6, no. 1 (January 2022): 5, https://doi.org/10.1038/s41529-021-00201-5.

8. O. F. Ngasoh, V. C. Anye, B. Agyei-Tuffour, O. K. Oyewole, P. A. Onwualu, and W. O. Soboyejo, "Corrosion Behavior of 5-Hydroxytryptophan (HTP)/Epoxy and Clay Particle-Reinforced Epoxy Composite Steel Coatings," *Cogent Engineering* 7, no. 1 (January 2020): 1797982, https://doi.org/10.1080/23311916.2020.1797982.

9. O. F. Ngasoh, A. Justine, M. Paul, D. K. Yusuf, B. A. Madugu, and E. E. Elachi, "Mechanical Properties of Epoxy/Clay Composite Coatings on an X65 Steel Substrate," *Cogent Engineering* 8, no. 1 (January 2021): https://doi.org/10.1080/23311916.2021.1944015.

10. J. I. Emmanuel, "Assessment of Internal and External Corrosion Control Measures for Crude Oil Transmission Pipelines for Asset Integrity Management," in *Asset Management Conference 2014, Institution of Engineering and Technology*, no. 7 (2014), 2.05, https://doi.org/10.1049/cp.2014.1035.

11. J. I. Emmanuel, "Application of 5-M Approach to Control Internal Corrosion for Crude Oil Transmission Pipelines," in *The NACE International Annual Conference (NACE)* (March 2016).

12. J. I. Emmanuel, *Risk-Based Internal Corrosion Control* (CORCON, 2021).

13. J. I. Emmanuel and T. T. Shaapere, "SPE-192938-MS Sulphate Reducing Bacteria SRB Control and Risk Based SRB Severity Ranking," (2018), http://onepetro.org/SPEADIP/proceedings-pdf/18ADIP/4-18ADIP/D041S096R004/1200326/spe-192938-ms.pdf/1.

14. J. I. Emmanuel, F. O. Ngasoh, A. Bello, P. A. Onwualu, and V. C. Anye, "Recent Advancements in Corrosion Inhibitor Performance Evaluation and Surface Analysis," in *2023 2nd International Conference on Multidisciplinary Engineering and Applied Science (ICMEAS)* (IEEE, November 2023), 1–6, https://doi.org/10.1109/ICMEAS58693.2023.10429879.

15. L. Guo, I. B. Obot, X. Zheng, et al., "Theoretical Insight Into an Empirical Rule About Organic Corrosion Inhibitors Containing Nitrogen, Oxygen, and Sulphur Atoms," *Applied Surface Science* 406 (June 2017): 301–306, https://doi.org/10.1016/j.apsusc.2017.02.134.

16. N. O. Obi-Egbedi, I. B. Obot, M. I. El-Khaiary, S. A. Umoren, and E. E. Ebenso, "Computational Simulation and Statistical Analysis on the Relationship Between Corrosion Inhibition Efficiency and Molecular Structure of Some Phenanthroline Derivatives on Mild Steel Surface," (2011), https://www.electrochemsci.org.

17. M. Kumar Karnena, M. Konni, S. Dash, et al., "Feasibility of Azadirachta Indica as a Green Inhibitor for Corrosion: A Preliminary Study," *Natural Volatiles and Essential Oils* 8, no. 5 (2021): 9312–9327.

18. P. C. Agu and K. Okon, "The Inhibition of Mild Steel Corrosion by Papaya and Neem Extracts," *Zastita Materijala* 64, no. 3 (September 2023): 274–282, https://doi.org/10.5937/zasmat2303274N.

19. B. Valdez-Salas, R. Vazquez-Delgado, J. Salvador-Carlos, et al., "Azadirachta Indica Leaf Extract as Green Corrosion Inhibitor for Reinforced Concrete Structures: Corrosion Effectiveness Against Commercial Corrosion Inhibitors and Concrete Integrity," *Materials* 14, no. 12 (June 2021): 3326, https://doi.org/10.3390/ma14123326.

20. Y. Fang, B. Suganthan, and R. P. Ramasamy, "Electrochemical Characterization of Aromatic Corrosion Inhibitors From Plant Extracts," *Journal of Electroanalytical Chemistry* 840 (May 2019): 74–83, https://doi.org/10.1016/j.jelechem.2019.03.052.

21. F. L. Halilova and R. M. Aligulyev, "Inhibition Effect of Tetraethanol-b-Octadecenyl Succinylamide in Acidic Corrosion of Carbonized Steel," *Eurasian Chemico-Technological Journal* 2, no. 2 (April 2016): 149–156, https://doi.org/10.18321/ectj372.

22. P. R. Sivakumar and A. P. Srikanth, "Green Corrosion Inhibitor: a Comparative Study," *Sadhana-Academy Proceedings in Engineering Sciences* 45, no. 1 (December 2020): 56, https://doi.org/10.1007/s12046-020-1283-x.

23. R. Idouhli, Y. Koumya, M. Khadiri, A. Aityoub, A. Abouelfida, and A. Benyaich, "Inhibitory Effect of Senecio Anteuphorbium as Green Corrosion Inhibitor for S300 Steel," *International Journal of Industrial Chemistry* 10, no. 2 (June 2019): 133–143, https://doi.org/10.1007/s40090-019-0179-2.

24. A. M. I. Inamuddin, M. Luqman, and T. Atalhi, "Sustainable Corrosion Inhibitors" (2021).

25. K. Tamalmani and H. Husin, *Review on Corrosion Inhibitors for Oil and Gas Corrosion Issues* (MDPI AG, 2020).

26. M. A. Quraishi and R. Sardar, "Aromatic Triazoles as Corrosion Inhibitors for Mild Steel in Acidic Environments," *Corrosion* 58, no. 9 (September 2002): 748–755, https://doi.org/10.5006/1.3277657.

27. N. Raghavendra, "Areca Plant Extracts as a Green Corrosion Inhibitor of Carbon Steel Metal in 3 M Hydrochloric Acid: Gasometric, Colorimetry and Atomic Absorption Spectroscopy Views," *Journal of Molecular and Engineering Materials* 6, no. 01n02 (March 2018): 1850004, https://doi.org/10.1142/s2251237318500041.

28. K. Srishailam, G. Ramesh, D. Praveena, et al., "Quantum Chemical Investigation of (E)-2-(2-Hydroxy-5-Methoxybenzylidene) Hydrazinecarbothioamide and Its N-Methyl Variant by Using DFT Methods," *Mathematical Analysis* (2024): https://doi.org/10.21203/rs.3.rs-3881706/v1.

29. J. M. Juma and S. A. H. Vuai, *Computational Studies of the Thermodynamic Properties, and Global and Reactivity Descriptors of Fluorescein Dye Derivatives in Acetonitrile Using Density Functional Theory* (SAGE Publications Ltd, 2021).

30. B. Gómez, N. V. Likhanova, M. A. Domínguez-Aguilar, R. Martínez-Palou, A. Vela, and J. L. Gázquez, "Quantum Chemical Study of the Inhibitive Properties of 2-Pyridyl-Azoles," *Journal of Physical Chemistry B* 110, no. 18 (May 2006): 8928–8934, https://doi.org/10.1021/jp057143y.

31. Y. Karzazi, M. E. Belghiti, F. El-Hajjaji, S. Boudra, and B. Hammouti, "Density Functional Theory Modelling and Monte Carlo Simulation Assessment of Inhibition Performance of Two Quinoxaline Derivatives for Steel Corrosion," *Journal of Materials and Environmental Science* 7, no. 11 (2016): 4011–4023.

32. T. Vinod Kumar, "Computational Studies for Inhibitory Action of 2-Mercapto-1-Methylimidazole Tautomers on Steel Using of Density Functional Theory Method (DFT)," *International Journal of Computational and Theoretical Chemistry* 4, no. 1 (2016): 1, https://doi.org/10.11648/j.ijctc.20160401.11.

33. A. Alija, D. Gashi, R. Plakaj, et al., "A Theoretical and Experimental Study of the Adsorptive Removal of Hexavalent Chromium Ions Using Graphene Oxide as an Adsorbent," *Open Chemistry* 18, no. 1 (August 2020): 936–942, https://doi.org/10.1515/chem-2020-0148.

34. A. Kouache, A. Khelifa, H. Boutoumi, et al., "Experimental and Theoretical Studies of *Inula viscosa* Extract as a Novel Eco-friendly Corrosion Inhibitor for Carbon Steel in 1 M Hcl," *Journal of Adhesion Science and Technology* 36, no. 9 (May 2022): 988–1016, https://doi.org/10.1080/01694243.2021.1956215.

35. B. Kosar and C. Albayrak, "Spectroscopic Investigations and Quantum Chemical Computational Study of (E)-4-Methoxy-2-[(p-Tolylimino) Methyl] Phenol," *Spectrochimica Acta Part A: Molecular and Biomolecular Spectroscopy* 78, no. 1 (January 2011): 160–167, https://doi.org/10.1016/j.saa.2010.09.016.

36. A. Abdouli, M. A. Djebbi, and A. Ben Haj Amara, "Synergistic Corrosion Inhibition and Controlled Release of Ascorbic Acid From a Layered Double Hydroxide Composite for Stainless Steel," *Journal of Electrochemical Science and Engineering* 15, no. 5 (July 2025): 2808, https://doi.org/10.5599/jese.2808.

37. A. Dehghani, A. H. Mostafatabar, G. Bahlakeh, and B. Ramezanzadeh, "A Detailed Study on the Synergistic Corrosion Inhibition Impact of the Quercetin Molecules and Trivalent Europium Salt on Mild Steel; Electrochemical/Surface Studies, DFT Modelling, and MC/MD Computer Simulation," *Journal of Molecular Liquids* 316 (October 2020): 113914, https://doi.org/10.1016/j.molliq.2020.113914.

38. T. Liang, H. Yuan, C. Li, et al., "Corrosion Inhibition Effect of Nano–SiO_2 for Galvanized Steel Superhydrophobic Surface," *Surface Coatings Technology* 406 (January 2021): 126673, https://doi.org/10.1016/j.surfcoat.2020.126673.

39. L. Ma, W. Lu, D. Yang, et al., "Dithiocarbamate Modified Glucose as a Novel Eco-Friendly Corrosion Inhibitor for Copper in Sodium Chloride Media," *Sustainable Chemistry and Pharmacy* 22 (September 2021): 100488, https://doi.org/10.1016/j.scp.2021.100488.

40. R. H. Aldahiri, M. A. Hussein, S. M. A. Al-Bukhari, K. A. Alamry, A. Khan, and R. Aslam, "Synergistic Effect of Canarium Strictum Leaves Extract and KI on the Corrosion Protection of Mild Steel in 15% Hcl Solution," *Scientific Reports* 15, no. 1 (December 2025): 3576, https://doi.org/10.1038/s41598-025-87482-x.

41. Y. Stiadi, "Synergistic Effect of Cinnamon (*Cinnamomum burmannii*) Leaves Extract and Potassium Iodide on Mild Steel in Hcl," *Chempublish Journal* 9, no. 1 (2025): 65–73, https://doi.org/10.22437/chp.v9i1.42334.

42. H. Hu, R. Feng, X. Ren, D. Wang, Y. Guo, and Z. Zhang, "Synergistic Corrosion Inhibition of 4-Hydroxypyridine and Halogen Ions: Insights From Interfacial Nonlinear Spectroscopy," *Journal of Chemical Physics* 161, no. 13 (October 2024): 134705, https://doi.org/10.1063/5.0230668.

43. Q. Zhang, Y. Yu, J. Li, et al., "Synergistic Corrosion Inhibition and UV Protection via TTA-Loaded LDH Nanocontainers in Epoxy Coatings," *Coatings* 15, no. 5 (April 2025): 505, https://doi.org/10.3390/coatings15050505.

44. S. Shadi, G. Bahlakeh, B. Ramezanzadeh, and A. H. J. Mofidabadi, "Experimental and Computational Exploration of Synergistic Effect of Laurus Nobilis Extract: Zinc Cation on Mild Steel Corrosion Inhibition in Saline Solution," *Journal of Molecular Liquids* 385 (September 2023): 122424, https://doi.org/10.1016/j.molliq.2023.122424.

45. D. A. Alwan and O. A. Hatem, "A Comprehensive Study on the Synergistic Effects of Cetyltrimethyl Ammonium Bromide and 1,2,4-Triazole as a Mild Steel Corrosion Inhibitor in an Acidic Environment," *Journal of Bio- and Tribo-Corrosion* 11, no. 2 (June 2025): 38, https://doi.org/10.1007/s40735-025-00947-4.

46. A. Nahlé, I. Abu-Abdoun, I. Abdel-Rahman, and M. Al-Khayat, "UAE Neem Extract as a Corrosion Inhibitor for Carbon Steel in Hcl Solution," *International Journal of Corrosion* 2010 (2010): 1–9, https://doi.org/10.1155/2010/460154.

47. A. S. Solanki, A. Sharma, S. Sharma, A. Thakur, and S. K. Sharma, "Mechanistic Investigation of Mild Steel Corrosion Inhibition by *Codiaeum variegatum* Extract: Weight Loss, EIS, and DFT Perspectives," *RSC Advances* 15, no. 30 (2025): 24202–24222, https://doi.org/10.1039/D5RA03125G.

48. A. Chandio, M. Kumar, U. Aftab, et al., "Experimental Study of Corrosion Inhibition of Carbon Steel in Acidic Environment Using Natural Guar Gum" (2023), https://doi.org/10.21203/rs.3.rs-2524306/v1.

49. F. El-Hajjaji, M. E. Belghiti, B. Hammouti, et al., "Adsorption and Corrosion Inhibition Effect of 2-Mercaptobenzimidazole (Surfactant) on a Carbon Steel Surface in an Acidic Medium: Experimental and Monte Carlo Simulations," *Portugaliae Electrochimica Acta* 36, no. 3 (March 2018): 197–212, https://doi.org/10.4152/pea.201803197.

50. A. Berisha, "Interactions Between the Aryldiazonium Cations and Graphene Oxide: A DFT Study," *Journal of Chemistry* 2019 (February 2019): 1–5, https://doi.org/10.1155/2019/5126071.

51. S. Kaya, L. Guo, C. Kaya, et al., "Quantum Chemical and Molecular Dynamic Simulation Studies for the Prediction of Inhibition Efficiencies of Some Piperidine Derivatives on the Corrosion of Iron," *Journal of the Taiwan Institute of Chemical Engineers* 65 (August 2016): 522–529, https://doi.org/10.1016/j.jtice.2016.05.034.

52. I. Lukovits, E. Kálmán, and F. Zucchi, "Corrosion Inhibitors—Correlation Between Electronic Structure and Efficiency," *Corrosion* 57, no. 1 (January 2001): 3–8, https://doi.org/10.5006/1.3290328.

53. D. Náfrádi and M. Kállay, "Self-Consistent Basis Set Extrapolation of Hartree–Fock Energies," *Structural Chemistry* 36 (June 2025): https://doi.org/10.1007/s11224-025-02542-2.

54. R. Oshima and H. Nakai, "Development of a Highly Efficient Convergence Method for Self-Consistent Field Calculations Combining Givens Rotation and Error Back-Propagation Algorithms," *Journal of Computer Chemistry* 24, no. 1 (Japan, 2025): 2025–0003, https://doi.org/10.2477/jccj.2025-0003.

55. N. A. Wazzan and F. M. Mahgoub, "DFT Calculations for Corrosion Inhibition of Ferrous Alloys by Pyrazolopyrimidine Derivatives," *Open Journal of Physical Chemistry* 04, no. 01 (2014): 6–14, https://doi.org/10.4236/ojpc.2014.41002.

56. A. H. Jabbar, Y. B. Theab, M. Soliyeva, et al., "Corrosion Protection Performance of Eco-Friendly Inhibitor for Zinc Metal Surface: Computational Modelling," *Chemical Physics* 598 (October 2025): 112812, https://doi.org/10.1016/j.chemphys.2025.112812.

57. D. A. Winkler, A. E. Hughes, C. Özkan, et al., "Impact of Inhibition Mechanisms, Automation, and Computational Models on the Discovery of Organic Corrosion Inhibitors," *Progress in Materials Science* 149 (March 2025): 101392, https://doi.org/10.1016/j.pmatsci.2024.101392.

58. V. K. R. Pulapa and M. R. Kotupalli, "Cyanthillium Cinerium (L.) Extract as Green Corrosion Inhibitor for Mild Steel in Acidic Medium: Electrochemical and Computational Study," *International Journal of Electrochemical Science* 20, no. 7 (July 2025): 101020, https://doi.org/10.1016/j.ijoes.2025.101020.

59. A. Samide, A. Dobriţescu, C. Tigae, C. I. Spînu, and B. Oprea, "Experimental and Computational Study on Inhibitory Effect and Adsorption Properties of N-Acetylcysteine Amino Acid in Acid Environment," *Molecules* 28, no. 19 (September 2023): 6799, https://doi.org/10.3390/molecules28196799.

60. H. M. Hassan, "Electrochemical and Computational Investigation of Cicer arietinum Extract as Renewable and Environmentally Green Corrosion Inhibitor for Aluminium in Acidic Environment," *Scientific Reports* 15, no. 1 (July 2025): 24864, https://doi.org/10.1038/s41598-025-96141-0.

61. A. Regti, H. Ben Elayouchia, M. El Haddad, and M. R. Laamari, "A Comparative Analysis of the Global Electrophilicity Power of Some Cationic Dyes. Understanding Selective Removal Dyes From Mixture Solution," *Letters in Applied NanoBioScience* 10, no. 4 (2021): 2933–2944, https://doi.org/10.33263/LIANBS104.29332944.

62. A. Y. Musa, A. A. H. Kadhum, A. B. Mohamad, A. A. B. Rahoma, and H. Mesmari, "Electrochemical and Quantum Chemical Calculations on 4,4-Dimethyloxazolidine-2-thIone as Inhibitor for Mild Steel Corrosion in Hydrochloric Acid," *Journal of Molecular Structure* 969, no. 1–3 (April 2010): 233–237, https://doi.org/10.1016/j.molstruc.2010.02.051.

63. E. Ahmed, M. Gad, J. H. Al-Fahemi, and E. A. M. Gad, "Adsorpitivity and Corrosion Inhibtion Performance of 2-(alkyloxy)-N, N, N-Tris(2-Hydroxyethyl)-2-Oxo-Ethanaminium Chloride Using DFT Approach," *Journal of Scientific and Engineering Research* 6, no. 10 (2015): http://www.ijser.org.

64. P. Geerlings and F. De Proft, "Chemical Reactivity as Described by Quantum Chemical Methods," *International Journal of Molecular Sciences* 3, no. 4 (April 2002): 276–309, https://doi.org/10.3390/i3040276.

65. L. Guo, Safi, S. Zaki, et al., "Anticorrosive Effects of Some Thiophene Derivatives Against the Corrosion of Iron: A Computational Study," *Frontiers of Chemistry* 6 (May 2018): 155, https://doi.org/10.3389/fchem.2018.00155.

66. I. B. Obot, D. D. Macdonald, and Z. M. Gasem, "Density Functional Theory (DFT) as a Powerful Tool for Designing New Organic Corrosion Inhibitors. Part 1: An Overview," *Corrosion Science* 99 (October 2015): 1–30, https://doi.org/10.1016/j.corsci.2015.01.037.

67. N. Kateris, R. Xu, and H. Wang, "HOMO-LUMO Energy Gaps of Complexes of Transition Metals With Single and Multi-Ring Aromatics," *Combustion and Flame* 257 (November 2023): 112513, https://doi.org/10.1016/j.combustflame.2022.112513.

68. D. Kumar, V. Jain, and B. Rai, "Understanding Synergistic Effects Between Corrosion Inhibitor Molecules Using Density Functional Theory," *Transactions of the Indian National Academy of Engineering* 8, no. 3 (September 2023): 403–409, https://doi.org/10.1007/s41403-023-00406-x.

69. P. Han, Y. He, C. Chen, et al., "Study on Synergistic Mechanism of Inhibitor Mixture Based on Electron Transfer Behavior," *Scientific Reports* 6, no. 1 (September 2016): 33252, https://doi.org/10.1038/srep33252.

70. A. Szabo and N. S. Ostlund, *Modern Quantum Chemistry: Introduction to Advanced Electronic Structure Theory* (Dover Publications, 1996).

71. J. Calais, "Density-Functional Theory of Atoms and Molecules," *International Journal of Quantum Chemistry* 47, no. 1 (July 1993): 101, https://doi.org/10.1002/qua.560470107.

72. P. Geerlings, F. De Proft, and W. Langenaeker, "Conceptual Density Functional Theory," *Chemistry Review* 103, no. 5 (May 2003): 1793–1874, https://doi.org/10.1021/cr990029p.

73. R. Chang and O. Jason, *Chemistry*, 13th ed. (McGraw Hill, 2017).

74. J. M. Juma and S. A. Vuai, "Computational Studies of the Thermodynamic Properties, and Global and Reactivity Descriptors of Fluorescein Dye Derivatives in Acetonitrile Using Density Functional Theory," *Journal of Chemical Research* 45, no. 7–8 (July 2021): 800–805, https://doi.org/10.1177/1747519821994518.

75. L. K. Caesar and N. B. Cech, "Synergy and Antagonism in Natural Product Extracts: when 1 + 1 Does Not Equal 2," *Natural Product Reports* 36, no. 6 (2019): 869–888, https://doi.org/10.1039/C9NP00011A.

76. R. Pezzani, B. Salehi, S. Vitalini, et al., "Synergistic Effects of Plant Derivatives and Conventional Chemotherapeutic Agents: An Update on the Cancer Perspective," *Medicina* 55, no. 4 (April 2019): 110, https://doi.org/10.3390/medicina55040110.

77. S. Gk, J. M. Jacob, and A. Raj, *Synergistic Effect of Salts on the Corrosion Inhibitive Action of Plant Extract: A Review* (Taylor and Francis Ltd, 2021).

78. S. A. Umoren, M. M. Solomon, I. B. Obot, and R. K. Suleiman, "A Critical Review on the Recent Studies on Plant Biomaterials as Corrosion Inhibitors for Industrial Metals," *Korean Society of Industrial Engineering Chemistry* 25 (August 2019): 91–115, https://doi.org/10.1016/j.jiec.2019.03.057.

79. U. Mamudu, M. S. Alnarabiji, and R. C. Lim, "Adsorption Isotherm and Molecular Modelling of Phytoconstituents From *Dillenia suffruticosa* Leaves for Corrosion Inhibition of Mild Steel in 1.0 M Hydrochloric Acid Solution," *Results in Surfaces and Interfaces* 13 (October 2023): 100145, https://doi.org/10.1016/j.rsurfi.2023.100145.

80. C. Verma, L. O. Olasunkanmi, E. E. Ebenso, M. A. Quraishi, and I. B. Obot, "Adsorption Behavior of Glucosamine-Based, Pyrimidine-Fused Heterocycles as Green Corrosion Inhibitors for Mild Steel: Experimental and Theoretical Studies," *Journal of Physical Chemistry C* 120, no. 21 (June 2016): 11598–11611, https://doi.org/10.1021/acs.jpcc.6b04429.

81. N. Mouats, S. Djellali, H. Ferkous, et al., "Comprehensive Investigation of the Adsorption, Corrosion Inhibitory Properties, and

Quantum Calculations for 2-(2,4,5-Trimethoxybenzylidene) Hydrazine Carbothioamide in Mitigating Corrosion of XC38 Carbon Steel Under Hcl Environment," *ACS Omega* 9, no. 26 (July 2024): 27945–27962, https://doi.org/10.1021/acsomega.3c10240.

82. M. L. Zheludkevich, D. G. Shchukin, K. A. Yasakau, H. Möhwald, and M. G. S. Ferreira, "Anticorrosion Coatings With Self-Healing Effect Based on Nanocontainers Impregnated With Corrosion Inhibitor," *Chemistry of Materials* 19, no. 3 (February 2007): 402–411, https://doi.org/10.1021/cm062066k.

83. X. Zuo, W. Li, W. Luo, et al., "Research of Lilium Brownii Leaves Extract as a Commendable and Green Inhibitor for X70 Steel Corrosion in Hydrochloric Acid," *Journal of Molecular Liquids* 321 (January 2021): 114914, https://doi.org/10.1016/j.molliq.2020.114914.

84. E. S. Junaid Ahmed and G. Mohan Ganesh, "Investigation of the Anti-Corrosion Effects of Azadirachta Indica Leaf Extract on Various Reinforcement Steels in 1 M Hcl: Results From Electrochemical, DFT and Simulation Studies," *Results in Engineering* 27 (September 2025): 105948, https://doi.org/10.1016/j.rineng.2025.105948.

85. R. S. Al-Moghrabi, A. M. Abdel-Gaber, and H. T. Rahal, "A Comparative Study on the Inhibitive Effect of Crataegus Oxyacantha and Prunus Avium Plant Leaf Extracts on the Corrosion of Mild Steel in Hydrochloric Acid Solution," *International Journal of Industrial Chemistry* 9, no. 3 (September 2018): 255–263, https://doi.org/10.1007/s40090-018-0154-3.

86. F. Cao, "Outstanding Synergistic Inhibition Effect of Ca 3 (PO 4) 2 and BTA on Q235 Steel in NaCl Solution," *Corrosion Engineering, Science and Technology: The International Journal of Corrosion Processes and Corrosion Control* (2025): https://doi.org/10.1177/1478422X251360180.

87. X. Teng, "Synergistic Corrosion Inhibition of Rubber Seed Extract With KI on Cold Rolled Steel in Sulfuric Acid Solution," *Journal of the Taiwan Institute of Chemical Engineers* 161 (2024): https://doi.org/10.1016/j.jtice.2024.105564.

88. C. Liao, "Insight Into Synergistic Corrosion Inhibition of Sodium Benzoate and Sodium Silicate on LZ91 Magnesium Alloy: Experimental and Theoretical Calculations," *Electrochimica Acta* 475 (2024): https://doi.org/10.1016/j.electacta.2023.143603.

Supporting Information

Additional supporting information can be found online in the Supporting Information section. *(Supporting Information)*

Graphical Abstract: "Drying and milling" refers to a standard, two-step preprocessing method for plant materials (leaves) where they are first dehydrated and then mechanically reduced to a fine, uniform powder. This technique is essential for ensuring homogeneity in samples, increasing the surface area for efficient compound extraction, and enhancing the stability of phytochemicals constituents. "Low-energy adsorption sites" suggest that the process is exothermic, facilitating the displacement of corrosive species by the phytochemical molecules. The computational study results were further corroborated using weight loss, EIS, and PDP, and the adsorption of GT 85 film on API 5L X65 was confirmed with FE-SEM and EDX analysis.

Appendix

A

TABLE A1 | A comprehensive review of the scientific studies on the synergistic interaction between 2024 and 2025.

Research area/limitations	Methods and maximum EI	Reference
Investigated the corrosion potential of raw *Codiaeum variegatum* extract *Study limitation* Studies were limited to only to performance of raw extracts and their phytochemicals	FTIR, WL, EIS, PDP, XPS, SEM EI: 91.83%	2025 [47]
Synergistic interaction of ascorbic acid (AA) intercalated into a MgAl layered double hydroxide (LDH) for protection of SS in HCl *Study limitation* Studies were limited to synergy between phytochemical and salt	RD, FTIR, SEM, TEM, EIS, DFT, MC EI: 70%	2025 [36]
Synergistic interaction of calcium phosphate [$Ca_3(PO_4)_2$] and benzotriazole (BTA) for protection of Q235 steel in 3.5 wt-% NaCl *Study limitation* Studies were limited to inhibition of inorganic mineral and synthetic organic compound	SEM-EDS, XPS, XRD, FTIR EI: 98.7%	2025 [86]
Synergistic interaction of epoxy/MgAl-TTA LDH@CeO2 coating *Study limitation* Limited to synergistic effects of resins and metal oxide without DFT and MC.	FTIR, UV-Vis, SEM, EIS EI: 89.87%	2025 [43]
Synergistic interaction of 1,2,4-triazole (TRI) and cetyltrimethylammonium bromide (CTAB). *Study limitation* Limited to synthetic quaternary ammonium salt interaction only without DFT and MC study	AFM, EIS, and PDP EI: 96.3%	2025 [45]
Synergistic interaction of *Canarium strictum* leaves (CSL) and KI for protection of mild steel (MS) in 15% HCl *Study limitation* Limited to synergistic inhibition of crude *Canarium strictum* extract using KI salts without DFT and MC analysis	Gravimetric, EIS, PDP, UV-Vis, FTIR, AFM, NMR, and SEM/EDS EI: 92.2%	2025 [40]
Synergistic interaction of potassium iodide and cinnamon leaf extract (CLE) for protection of MS in HCl *Study limitation* Limited to synergy between KI and CLE, without DFT and MC simulation of raw extract.	Gravimetric, UV-Vis, XRD EI: 97.06%	2025 [41]
Synergistic interaction of rubber seed extract (RSE) and KI for protection of cold-rolled steel (CRS) in sulfuric acid (H_2SO_4) *Study limitation* Limited to crude rubber seed extracts and KI interaction. No molecular level study of the phytochemicals (DFT and MC).	SEM/AFM, XPS, contact angle, FTIR, UV-Vis, LS-MS EI: 96.82%	2024 [87]
Synergistic effects of sodium benzoate and sodium silicate for protection of LZ91 magnesium alloy *Study limitation* Limited to synergistic effects of sodium benzoate and sodium silicate. Plant phytochemical was not studied.	FTIR, XPS, EIS EI: 92.3%	2024 [88]
Synergistic interaction of 4-mercapto/4-aminopyridine and 4-HPy with halogen ions for protection of MS in 0.5 mol/L HCl *Study limitation* Limited to phytochemical with ion interaction without DFT and MC analysis.	Harmonic generation (SHG) spectroscopy, combined with EIS, Raman spectroscopy, AFM, X-ray photoelectron spectroscopy, UV-Vis	NA [42]

Appendix

B

TABLE A2 | GS-MS data for golden palm and neem leaves.

Dypsis lutescens (golden palm)				*Azadirachta indica* (neem)			
Peak	**Retention time**	**Area**	**Library/ID**	**Peak**	**Retention time**	**Area**	**Library/ID**
1	5.7227	45.5502	D-Limonene	14	26.8675	0.3702	Bicyclo[3.1.1] heptane, 2,6,6-trimethyl-
2	15.0282	4.8999	9-Octadecene, (E)-	15	27.8002	3.5507	Dodecanoic acid, 10-methyl-, methyl ester
3	15.2249	6.4253	Hexadecane	16	28.6941	1.6113	Phthalic acid, ethyl pentadecyl ester
4	20.1796	8.4622	5-Octadecene, (E)-	17	29.1719	2.2869	10-Heneicosene (c,t)
5	20.3468	8.207	Hexadecane	18	29.282	1.146	2-Piperidinone, N-[4-bromo-n-butyl]-
6	24.886	15.8288	9-Eicosene, (E)-	19	31.0758	2.6439	17-Pentatriacontene
7	25.0223	6.8512	10-Methylnonadecane	20	31.2387	3.374	Methyl 10-trans,12-cis-octadecadienoate
8	27.7984	35.5358	Hexadecanoic acid, methyl ester	21	31.3529	5.3625	(Z)-Methyl heptadec-9-enoate
9	29.1676	23.6357	1-Docosene	22	31.4787	3.7653	Isopulegol
10	29.2774	7.7509	Hexadecane, 1-bromo-	23	31.6394	11.5163	Phytol
11	31.2435	5.5351	9-Octadecyne	24	31.8451	10.3589	Tetradecanoic acid, 12-methyl-, methyl ester, (S)-
12	31.3487	9.7132	6-Octadecenoic acid, methyl ester, (Z)-	25	32.0395	4.1721	Tetradecanal
13	31.8392	12.4032	Tetradecanoic acid, 12-methyl-, methyl ester, (S)-	26	32.1241	1.6804	E-9-Methyl-8-tridecen-2-ol, acetate
14	33.0818	24.4435	17-Pentatriacontene	27	32.2323	5.1656	2-Methyl-Z,Z-3,13-octadecadienol
15	34.297	8.806	Aspidospermidin-17-ol, 1-acetyl-19,21-epoxy-15,16-dimethoxy-	28	32.2923	2.9347	11-Tetradecyn-1-ol acetate
16	34.5468	4.2569	Heptadecanal	29	32.4184	4.4296	*trans*-2-Dodecen-1-ol
17	34.7089	4.5432	Aspidospermidin-17-ol, 1-acetyl-19,21-epoxy-15,16-dimethoxy-	30	32.4528	1.6009	Z-2-Tridecen-1-ol
18	35.6315	7.8273	Octadecanal	31	32.5481	6.0021	Tetradecanal
19	36.1306	9.9817	Undec-10-ynoic acid, tetradecyl ester	32	32.6421	14.3868	Z-2-Octadecen-1-ol
20	36.215	2.1205	Heptadecanoic acid, heptadecyl ester	33	33.0774	2.2787	Pentafluoropropionic acid, hexadecyl ester
21	36.269	1.8908	(E)-pent-2-en-3-yl hexanoate	34	37.6377	−0.1295	Octacosyl trifluoroacetate
22	36.7084	27.8236	Heptadecyl heptafluorobutyrate	35	37.8539	0.9628	Cyclopentane, (2-methylpropyl)-
23	36.825	8.0231	Heptadecanoic acid, heptadecyl ester	36	37.9984	0.4262	17-Pentatriacontene
24	38.2097	−267.2605	Cyclononasiloxane, octadecamethyl-	37	38.3997	0.2416	*cis*-(−)-1,2-Epoxy-*p*-menth-8-ene
25	38.5169	76.7454	6,11-Dimethyl-2,6,10-dodecatrien-1-ol	38	38.5169	1.8052	2,6,10,14,18-Pentamethyl-2,6,10,14,18-eicosapentaene

Appendix

C

TABLE A3 | FTIR data for golden palm and neem.

Dypsis lutescens (golden palm)				*Azadirachta indica* (neem)			
Peak	**Wavenumber (cm^{-1})**	**Vibration/ bond**	**Functional group**	**Peak**	**Wavenumber (cm^{-1})**	**Vibration/ bond**	**Functional group**
1	1013.83589	C-O	Alcohols, carboxylic acids, esters, and ethers	1	1320–1000	C-O	Alcohols, carboxylic acids, esters, and ethers
2	1110.74668	C-O	Alcohols, carboxylic acids, esters, and ethers	2	1320–1000	C-O	Alcohols, carboxylic acids, esters, and ethers
3	1446.20708	C–H Bend	Alkanes (methyl)	3	1550 and 1350 (s)	N=O	Nitro (R–NO2)
4	1654.938	C=C stretch	Alkene	4	1670–1640 (s)	C=O	Amide
5	2124.58257	C ≡ C stretch	Alkyne	5	3400–2400	O-H	Carboxylic Acids
6	2832.77676	C–H stretch	Alkanes (Aldehyde)	6	2850 and 2750 (w)	C–H (Aldehyde)	Alkanes (Aldehyde)
7	2944.59689	C–H stretch	Alkanes	7	3000–2850	C–H stretch	Alkanes (Aldehyde)
8	3294.96665	N–H stretch	1°, 2° amines and amides	8	3400–3250	N–H stretch	1°, 2° amines and amides

Appendix

D

Monte Carlo simulation (kcal/mol) data for individual Nine (9) at 30% Water Cut, 50% Water Cut, and 70% Water Cut ((1-Docosene; 1DO, 6,11-Dimethyl-2,6,10-dodecatrien-1-ol, methyl ester (Z); 6,11DIM, 9-Eicosene; 9EI, 17-Pentatriacontene; 17PEN, heptadecyl heptafluorobutyrate; HEP, D-limonene; DLM, n-hexadecenoic acid; nHXA, tetradecanoic acid; TTD, Z-2-Octadecen-1-ol; Z2OT) phytochemicals during annealing (adsorption) on Fe (111) system.

TABLE A4 | Monte carlo simulation (kcal/mol) data for individual Nine (9) at 30 % water cut, 50% water cut, and 70% water cut ((1-docosene; 1DO, 6,11-dimethyl-2,6,10-dodecatrien-1-ol, methyl ester (Z); 6,11DIM, 9eicosene; 9EI, 17-pentatriacontene; 17PEN, heptadecyl heptafluorobutyrate; HEP, D-limonene; DLM, n-hexadecenoic acid; nHXA, tetradecanoic acid; TTD, Z-2-octadecen-1-ol; Z2OT) phytochemicals during annealing (adsorption) on Fe (111) system.

Water cuts	**Structures**	**Total energy (kcal/mol)**	**Adsorption energy (kcal/mol)**	**Rigid adsorption energy (kcal/mol)**	**Deformation energy (kcal/mol)**
30% Water Cut	Fe (2) (1 1 1)-12	−6240.62	−4587.24	−4383.71	−203.528
50% Water Cut	Fe (2) (1 1 1)-22	−5857.38	−4968.04	−4575.65	−392.394
70% Water Cut	Fe (2) (1 1 1)-37	−5497.81	−5372.52	−4756.7	−615.818
Water cuts		**1DO: dEad/dNi (kcal/mol)**	**H_2O: dEad/dNi (kcal/mol)**	**HCL: dEad/dNi (kcal/mol)**	**LAWS: dEad/dNi (kcal/mol)**
30% Water Cut	Fe (2) (1 1 1)-12	−187.351	−75.0908	−9.6639	−44.0277
50% Water Cut	Fe (2) (1 1 1)-22	−118.145	−71.7913	−8.99791	−55.2336
70% Water Cut	Fe (2) (1 1 1)-37	−73.2838	−63.4853	−10.9889	−45.1467
Water cuts	**Structures**	**Total energy (kcal/mol)**	**Adsorption energy (kcal/mol)**	**Rigid adsorption energy (kcal/mol)**	**Deformation energy (kcal/mol)**
30% Water Cut	Fe (1 1 1)-15	−6108.76	−4487.33	−4299.18	−188.153
50% Water Cut	Fe (1 1 1)-8	−5898.74	−5042.83	−4619.16	−423.666
70% Water Cut	Fe (1 1 1)-5	−5690.11	−5599.69	−4967.1	−632.591
Water cuts		**6,11DIM: dEad/dNi (kcal/mol)**	**H_2O: dEad/dNi (kcal/mol)**	**HCL: dEad/dNi (kcal/mol)**	**LAWS: dEad/dNi (kcal/mol)**
30% Water Cut	Fe (1 1 1)-15	−167.976	−81.5591	−13.7118	−42.5465

(Continues)

TABLE A4 | (Continued)

50% Water Cut	Fe (1 1 1)-8	−146.502	−73.6561	−11.4912	−51.1693
70% Water Cut	Fe (1 1 1)-5	−127.247	−71.6205	−13.3263	−58.8354
Water cuts	**Structures**	**Total energy (kcal/mol)**	**Adsorption energy (kcal/mol)**	**Rigid adsorption energy (kcal/mol)**	**Deformation energy (kcal/mol)**
30% Water Cut	Fe (1 1 1)-21	−5847.04	−4198.34	−3952.87	−245.471
50% Water Cut	Fe (1 1 1)-18	−5854.18	−4970.99	−4580.31	−390.673
70% Water Cut	Fe (1 1 1)-8	−5621.2	−5503.51	−4899.24	−604.276
Water cuts		**9EI: dEad/dNi (kcal/mol)**	**H_2O: dEad/dNi (kcal/mol)**	**HCL: dEad/dNi (kcal/mol)**	**LAWS: dEad/dNi (kcal/mol)**
30% Water Cut	Fe (1 1 1)-21	−164.341	−47.9809	−11.3928	−39.8028
50% Water Cut	Fe (1 1 1)-18	−82.2374	−75.1704	−12.3545	−51.0569
70% Water Cut	Fe (1 1 1)-8	−97.4245	−77.8643	−11.0346	−54.0654
Water cuts	**Structures**	**Total energy (kcal/mol)**	**Adsorption energy (kcal/mol)**	**Rigid adsorption energy (kcal/mol)**	**Deformation energy (kcal/mol)**
30% Water Cut	Fe (1 1 1)-30	−6103.96	−4426.88	−4212.2	−214.679
50% Water Cut	Fe (1 1 1)-13	−5917.07	−5005.51	−4580.24	−425.267
70% Water Cut	Fe (1 1 1)-21	−5620.49	−5474.43	−4872.26	−602.171
Water cuts		**17PEN: dEad/dNi (kcal/mol)**	**H_2O: dEad/dNi (kcal/mol)**	**HCL: dEad/dNi (kcal/mol)**	**LAWS: dEad/dNi (kcal/mol)**
30% Water Cut	Fe (1 1 1)-30	−228.373	−75.2795	−13.3576	−52.4944
50% Water Cut	Fe (1 1 1)-13	−248.8	−70.0439	−13.8752	−47.2209
70% Water Cut	Fe (1 1 1)-21	−178.045	−71.6186	−10.1407	−45.8527
Water cuts	**Structures**	**Total energy (kcal/mol)**	**Adsorption energy (kcal/mol)**	**Rigid adsorption energy (kcal/mol)**	**Deformation energy (kcal/mol)**
30% Water Cut	Fe (1 1 1)-2	−6211.82	−4586.48	−4379.68	−206.799
50% Water Cut	Fe (1 1 1)-18	−5750.75	−4890.92	−4502.7	−388.218
70% Water Cut	Fe (1 1 1)-7	−5568.44	−5474.11	−4861	−613.115
Water cuts		**DLM: dEad/dNi (kcal/mol)**	**H_2O: dEad/dNi (kcal/mol)**	**HCL: dEad/dNi (kcal/mol)**	**LAWS: dEad/dNi (kcal/mol)**
30% Water Cut	Fe (1 1 1)-2	−103.561	−89.793	−12.4573	−41.2339
50% Water Cut	Fe (1 1 1)-18	−76.5556	−74.9401	−13.968	−41.2225
70% Water Cut	Fe (1 1 1)-7	−51.323	−74.6031	−12.8657	−56.5755
Water cuts	**Structures**	**Total energy (kcal/mol)**	**Adsorption energy (kcal/mol)**	**Rigid adsorption energy (kcal/mol)**	**Deformation energy (kcal/mol)**
30% Water Cut	Fe (1 1 1)-25	−5882.59	−5035.68	−4623.59	−412.087

(Continues)

TABLE A4 | (Continued)

50% Water Cut	Fe (1 1 1)-7	−5568.44	−5474.11	−4861	−613.115
70% Water Cut	Fe (1 1 1)-20	−5618.52	−5537.12	−4931.21	−605.904
Water cuts		**HEP: dEad/dNi (kcal/mol)**	**H_2O: dEad/dNi (kcal/mol)**	**HCL: dEad/dNi (kcal/mol)**	**LAWS: dEad/dNi (kcal/mol)**
30% Water Cut	Fe (1 1 1)-25	−285.064	−77.9203	−11.6308	−46.8476
50% Water Cut	Fe (1 1 1)-7	−51.323	−74.6031	−12.8657	−56.5755
70% Water Cut	Fe (1 1 1)-20	−280.817	−75.6939	−15.5614	−51.1594
Water cuts	**Structures**	**Total energy (kcal/mol)**	**Adsorption energy (kcal/mol)**	**Rigid adsorption energy (kcal/mol)**	**Deformation energy (kcal/mol)**
30% Water Cut	Fe (1 1 1)-22	−6103.08	−4431.73	−4239	−192.73
50% Water Cut	Fe (1 1 1)-11	−5874.79	−4968.95	−4556.69	−412.261
70% Water Cut	Fe (1 1 1)-11	−5588.52	−5448.18	−4830.9	−617.28
Water cuts		**HXA: dEad/dNi (kcal/mol)**	**H_2O OP: dEad/dNi (kcal/mol)**	**HCL OP: dEad/dNi (kcal/mol)**	**LAWS OP: dEad/dNi (kcal/mol)**
30% Water Cut	Fe (1 1 1)-22	−264.098	−69.3344	−12.0747	−44.965
50% Water Cut	Fe (1 1 1)-11	−132.856	−80.7891	−11.969	−39.2035
70% Water Cut	Fe (1 1 1)-11	−276.558	−75.5787	−13.8311	−53.9949
Water cuts	**Structures**	**Total energy (kcal/mol)**	**Adsorption energy (kcal/mol)**	**Rigid adsorption energy (kcal/mol)**	**Deformation energy (kcal/mol)**
30% Water Cut	Fe (1 1 1)-66	−5987.79	−4359.32	−4131.59	−227.732
50% Water Cut	Fe (1 1 1)-9	−5760.04	−4897.08	−4511.24	−385.838
70% Water Cut	Fe (1 1 1)-2	−5167.02	−5069.56	−4419.8	−649.759
Water cuts		**TTDMS: dEad/dNi (kcal/mol)**	**H_2O: dEad/dNi (kcal/mol)**	**HCL: dEad/dNi (kcal/mol)**	**LAWS: dEad/dNi (kcal/mol)**
30% Water Cut	Fe (1 1 1)-66	−176.615	−82.458	−9.9505	−41.2171
50% Water Cut	Fe (1 1 1)-9	−103.743	−81.9355	−8.65036	−54.0132
70% Water Cut	Fe (1 1 1)-2	−220.117	−31.7128	−8.45516	−33.7168
Water cuts	**Structures**	**Total energy (kcal/mol)**	**Adsorption energy (kcal/mol)**	**Rigid adsorption energy (kcal/mol)**	**Deformation energy (kcal/mol)**
30% Water Cut	Fe (1 1 1)-7	−6161	−4130.17	−4338.11	207.9325
50% Water Cut	Fe (1 1 1)-28	−5917.09	−4456.26	−4631.13	174.8697
70% Water Cut	Fe (1 1 1)-26	−5666.22	−4775.39	−4970.8	195.4097
Water cuts		**Z2OT: dEad/dNi (kcal/mol)**	**H_2O: dEad/dNi (kcal/mol)**	**HCL: dEad/dNi (kcal/mol)**	**LAWS: dEad/dNi (kcal/mol)**
30% Water Cut	Fe (1 1 1)-7	−193.567	−76.4367	−14.6218	−42.2537
50% Water Cut	Fe (1 1 1)-28	−141.199	−61.5932	−11.2298	−50.5272
70% Water Cut	Fe (1 1 1)-26	−174.587	−68.3111	−10.7171	−56.3846

Appendix

E

Monte Carlo Simulation (kcal/mol) data for combined Nine (9) Phytochemicals ((1-Docosene; 1DO, 6,11-Dimethyl-2,6,10-dodecatrien-1-ol, methyl ester (Z); 6,11DIM, 9-Eicosene; 9EI, 17-Pentatriacontene; 17PEN, Heptadecyl heptafluorobutyrate; HEP, D-Limonene; DLM, n-Hexadecenoic acid; nHXA, Tetradecanoic acid; TTD, Z-2-Octadecen-1-ol; Z2OT) phytochemicals during annealing (Adsorption) on Fe (111) system.

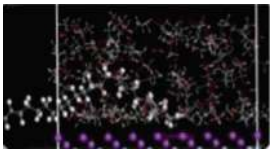
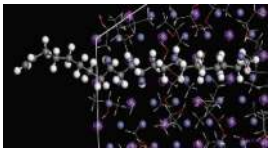
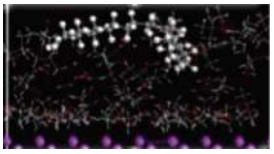
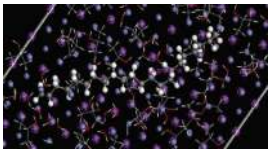
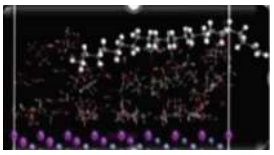
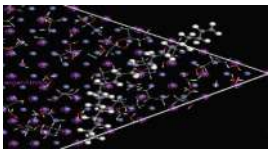
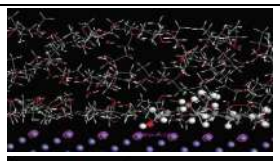
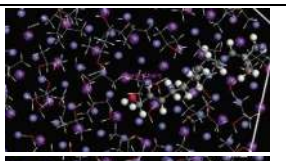
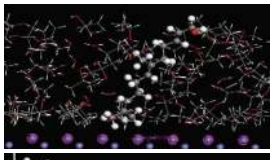
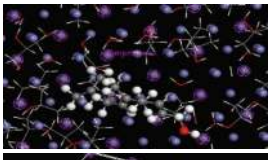
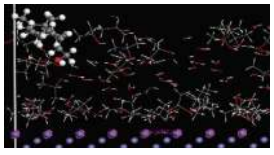
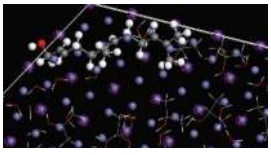
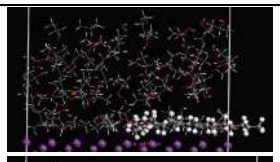
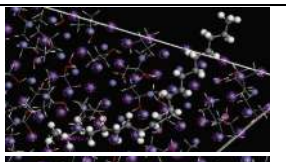
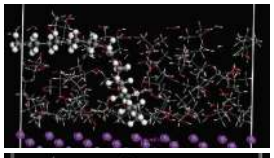
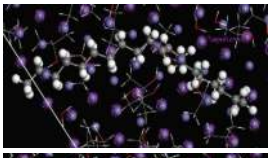
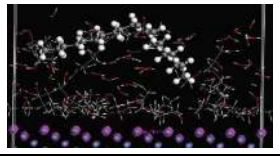
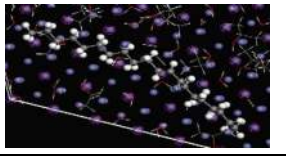
TABLE A5 | Monte carlo simulation (kcal /mol) data for combined nine (9) phytochemicals ((1-dcosene; 1DO, 6,11-dimethyl-2,6,10-dodecatrien-1-ol, methyl ester (Z); 6,11DIM, 9-eicosene; 9EI, 17-pentatriacontene; 17PEN, heptadecyl heptafluorobutyrate; HEP, D-limonene; DLM, n-hexadecenoic acid; nHXA, tetradecanoic acid; TTD, Z-2-Octadecen-1-ol; Z2OT) phytochemicals during annealing (Adsorption) on Fe (111) system.

Structures	Total energy (kcal/mol)	Adsorption energy (kcal/mol)	Rigid adsorption energy (kcal/mol)	Deformation energy (kcal/mol)	Z2OT: dEad/dNi (kcal/mol)	nHXA: dEad/dNi (kcal/mol)	DLM: dEad/dNi (kcal/mol)
Fe (1 1 1) - 33	−6314.030	−4472.220	−4208.430	−263.798	−77.8779	−203.11	−43.9824
HEP: dEad/dNi (kcal/mol)	**1DO: dEad/dNi (kcal/mol)**	**9EI: dEad/dNi (kcal/mol)**	**TTD: dEad/dNi (kcal/mol)**	**H_2O: dEad/dNi (kcal/mol)**	**HCL: dEad/dNi (kcal/mol)**	**LAWS: dEad/dNi (kcal/mol)**	**6,11-DIM: dEad/dNi (kcal/mol)**
−140.267	−208.301	−138.128	−127.561	−59.606	−9.917	−35.097	−156.252

Appendix

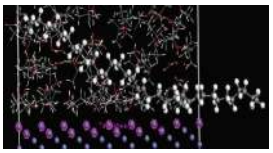
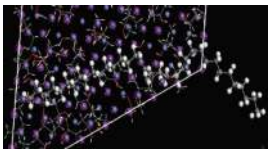
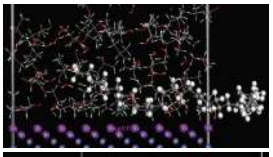
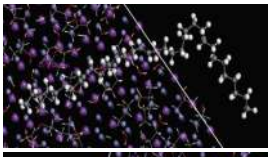
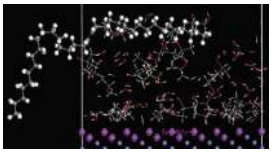
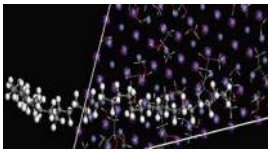
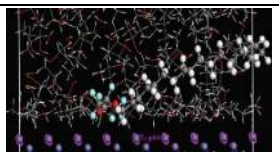
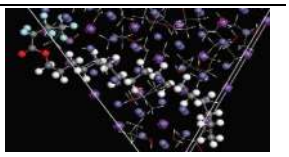
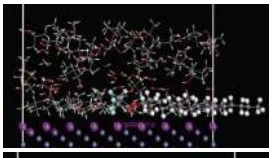
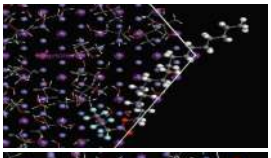
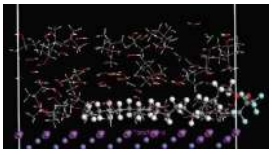
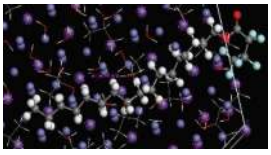
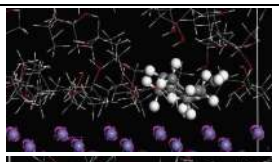
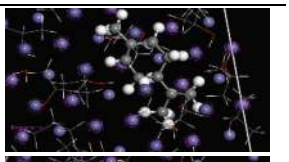
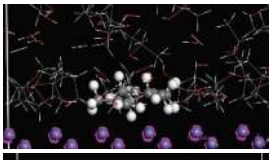
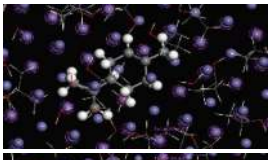
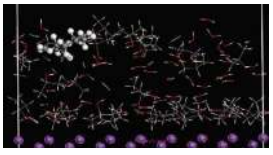
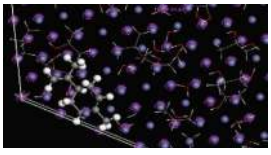
F

TABLE A6 | (a–i) Front and top views of the stable adsorption configuration of phytochemicals on the Fe (111) interface in 30%, 50%, and 70% water-cut systems, obtained using the adsorption locator module in the compass force field.

Phytochemicals	Front view		Top view	
1-Docosene (a)	Front View (30% Water Cut)		Top View (30% Water Cut)	
	Front View (50% Water Cut)		Top View (50% Water Cut)	
	Front View (70% Water Cut)		Top View (70% Water Cut)	
6,11-Dimethyl-2,6,10-dodecatrien-1-ol, methyl ester (*Z*) (b)	Front View (30% Water Cut)		Top View (30% Water Cut)	
	Front View (50% Water Cut)		Top View (50% Water Cut)	
	Front View (70% Water Cut)		Top View (70% Water Cut)	
9-Eicosene (c)	Front View (30% Water Cut)		Top View (30% Water Cut)	
	Front View (50% Water Cut)		Top View (50% Water Cut)	
	Front View (70% Water Cut)		Top View (70% Water Cut)	

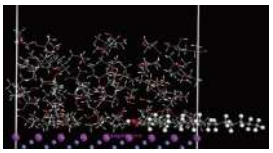
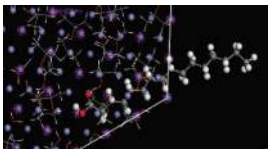
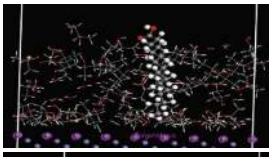
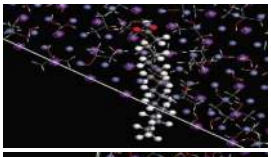
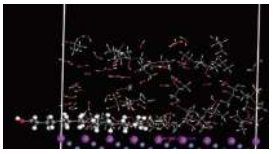
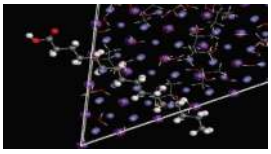
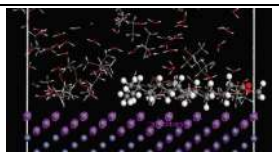
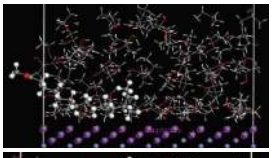
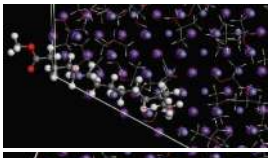
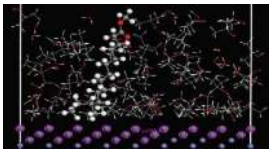
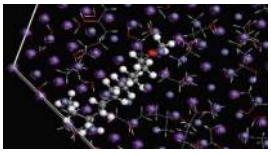
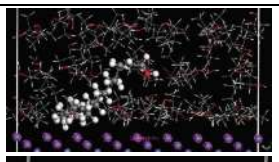
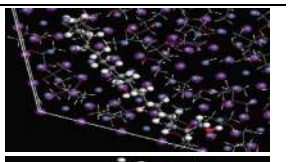
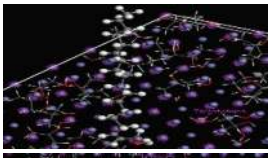
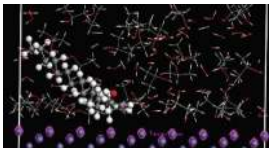
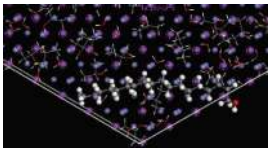
(Continues)

TABLE A6 | (Continued)

Phytochemicals	Front view		Top view	
17-Pentatriacontene (d)	Front View (30% Water Cut)		Top View (30% Water Cut)	
	Front View (50% Water Cut)		Top View (50% Water Cut)	
	Front View (70% Water Cut)		Top View (70% Water Cut)	
Heptadecyl heptafluorobutyrate (e)	Front View (30% Water Cut)		Top View (30% Water Cut)	
	Front View (50% Water Cut)		Top View (50% Water Cut)	
	Front View (70% Water Cut)		Top View (70% Water Cut)	
D-Limonene (f)	Front View (30% Water Cut)		Front View (30% Water Cut)	
	Front View (50% Water Cut)		Front View (50% Water Cut)	
	Front View (70% Water Cut)		Front View (70% Water Cut)	

(Continues)

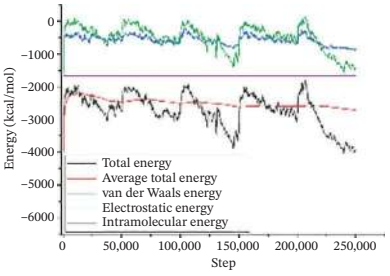
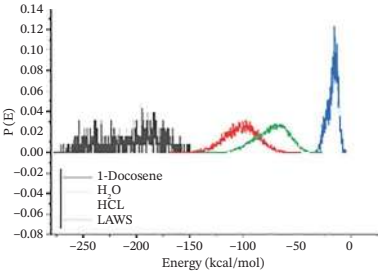
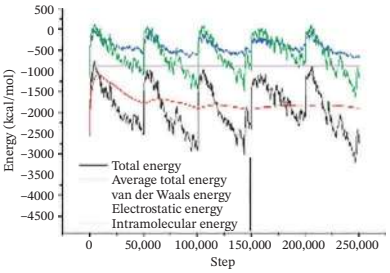
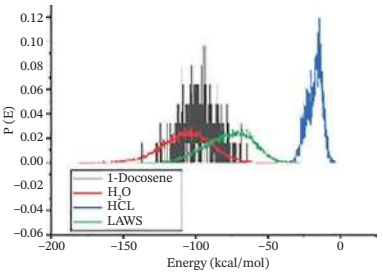
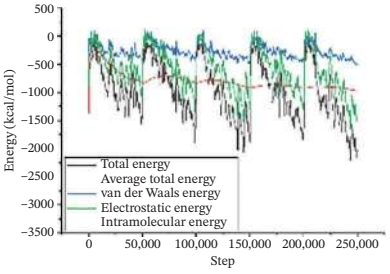
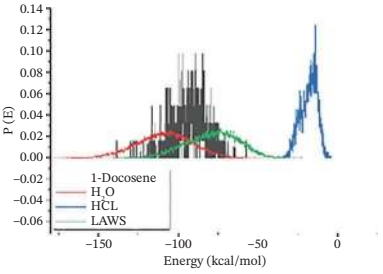
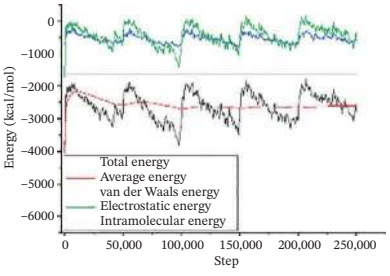
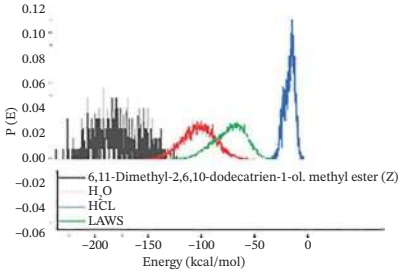
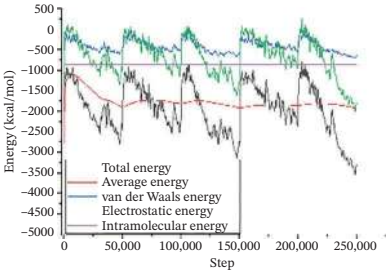
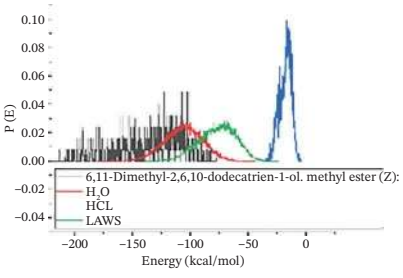
TABLE A6 | (Continued)

Phytochemicals	Front view		Top view	
n-Hexadecenoic acid (g)	Front View (30% Water Cut)		Front View (30% Water Cut)	
	Front View (50% Water Cut)		Front View (50% Water Cut)	
	Front View (70% Water Cut)		Front View (70% Water Cut)	
Tetradecanoic acid (h)	Front View (30% Water Cut)		Front View (30% Water Cut)	
	Front View (50% Water Cut)		Front View (50% Water Cut)	
	Front View (70% Water Cut)		Front View (70% Water Cut)	
Z-2-Octadecen-1-ol; Z2OT (i)	Front View (30% Water Cut)		Front View (30% Water Cut)	
	Front View (50% Water Cut)		Front View (50% Water Cut)	
	Front View (70% Water Cut)		Front View (70% Water Cut)	

Appendix

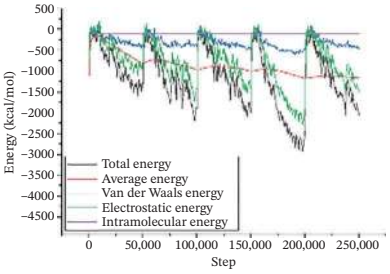
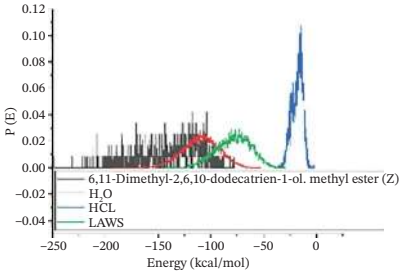
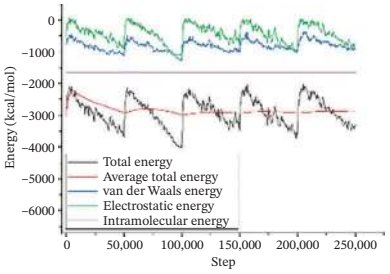
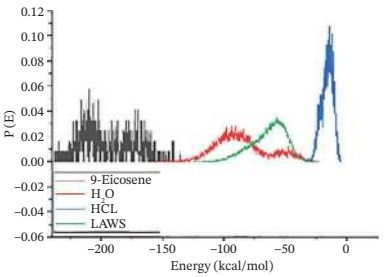
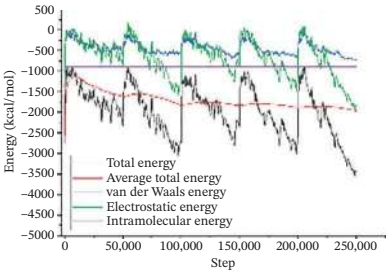
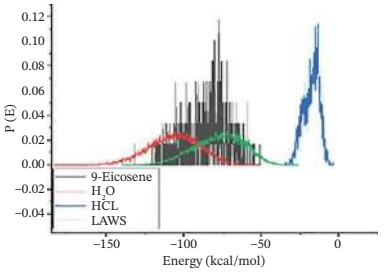
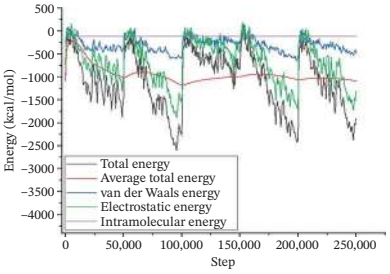
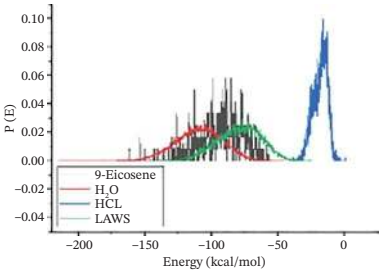
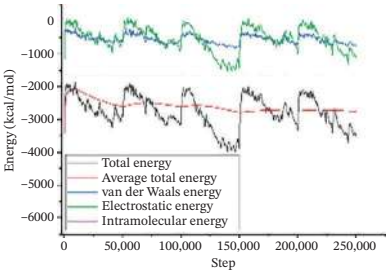
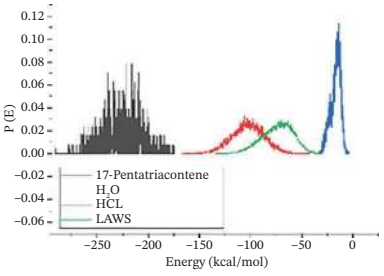
G

TABLE A7 | (a–i) Contribution of various energy forms and distribution of adsorption energies obtained from Monte Carlo (MC) simulations for nine phytochemicals.

Phytochemicals	Contribution of the different energy types during the MC calculations for iron (Fe) (111)	Distribution of the adsorption energies on the iron (Fe) (111)
1-Docosene (a)		
30% Water Cut (21 $H_2$0/9 HCl/70 LAWS system		
50% Water Cut (41 $H_2$0/9 HCl/50 LAWS system		
70% Water Cut (61 $H_2$0/9 HCl/30 LAWS system		
6,11-Dimethyl-2,6,10-dodecatrien-1-ol, methyl ester (Z) (b)		
30% Water Cut (21 $H_2$0/9 HCl/70 LAWS system		
50% Water Cut (41 $H_2$0/9 HCl/50 LAWS system		

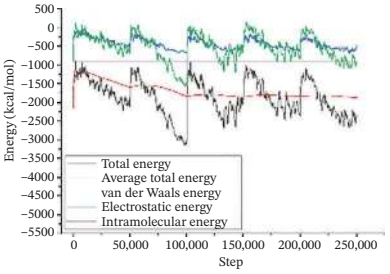
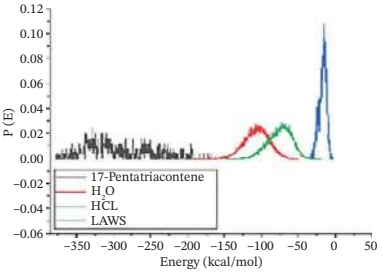
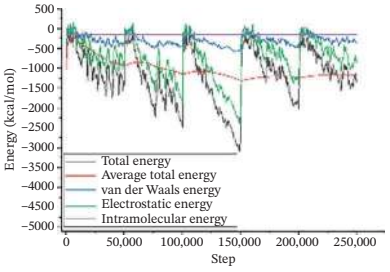
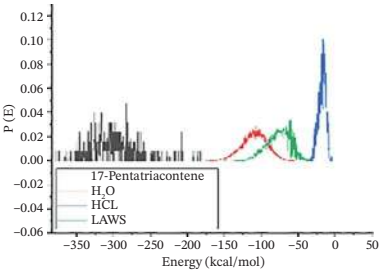
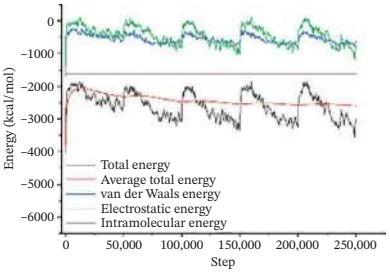
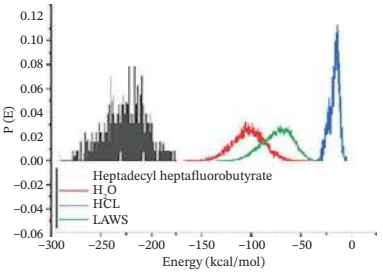
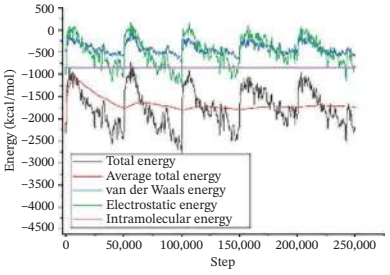
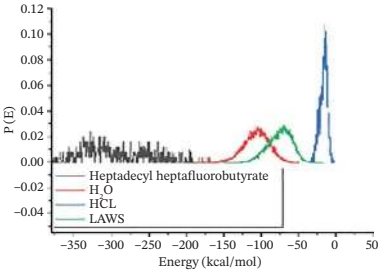
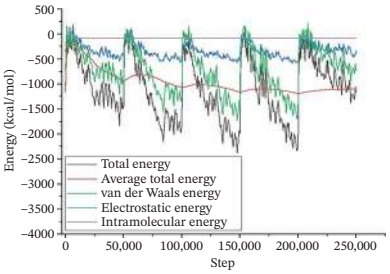
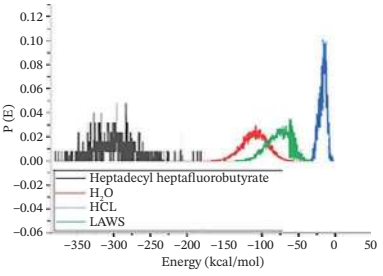
(Continues)

TABLE A7 | (Continued)

Phytochemicals	Contribution of the different energy types during the MC calculations for iron (Fe) (111)	Distribution of the adsorption energies on the iron (Fe) (111)
70% Water Cut (61 H_20/9 HCl/30 LAWS system		
9-Eicosene (c)		
30% Water Cut (21 H_20/9 HCl/70 LAWS system		
50% Water Cut (41 H_20/9 HCl/50 LAWS system		
70% Water Cut (61 H_20/9 HCl/30 LAWS system		
17-Pentatriacontene (d)		
30% Water Cut (21 H_20/9 HCl/70 LAWS system		

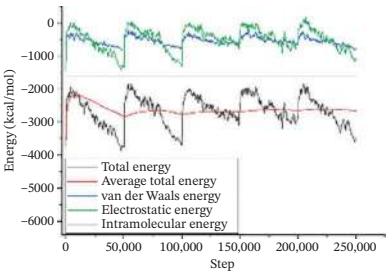
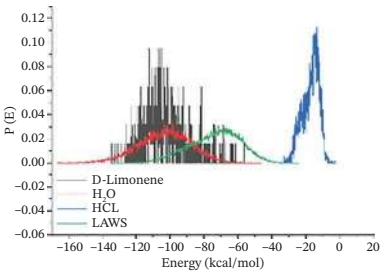
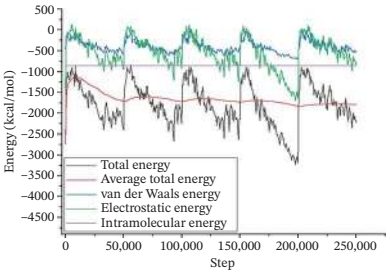
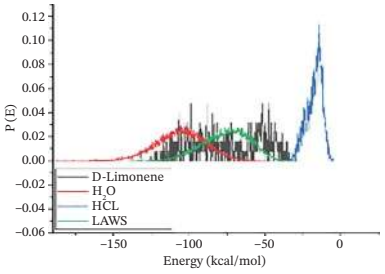
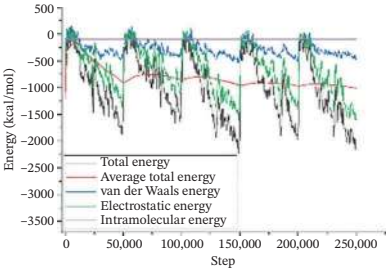
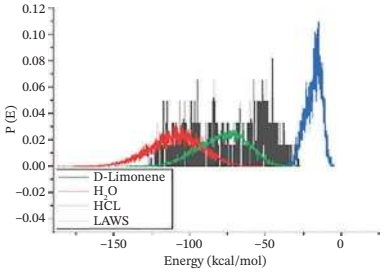
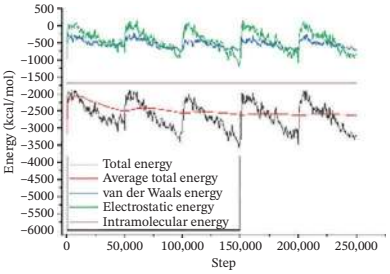
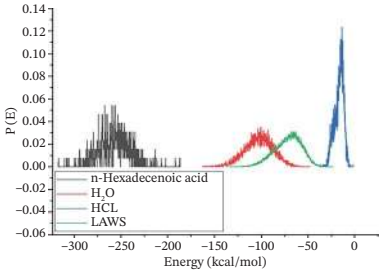
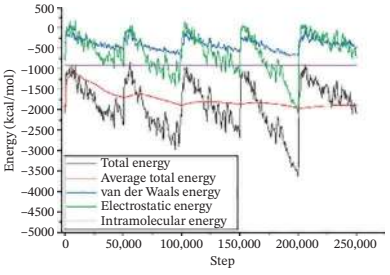
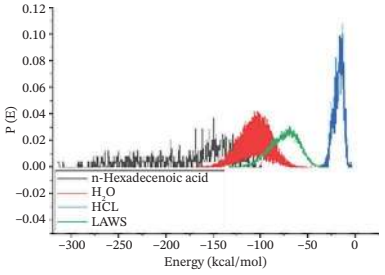
(Continues)

TABLE A7 | (Continued)

Phytochemicals	Contribution of the different energy types during the MC calculations for iron (Fe) (111)	Distribution of the adsorption energies on the iron (Fe) (111)
50% Water Cut (41 H_20/9 HCl/50 LAWS system		
70% Water Cut (61 H_20/9 HCl/30 LAWS system		
Heptadecyl heptafluorobutyrate (e)		
30% Water Cut (21 H_20/9 HCl/70 LAWS system		
50% Water Cut (41 H_20/9 HCl/50 LAWS system		
70% Water Cut (61 H_20/9 HCl/30 LAWS system		

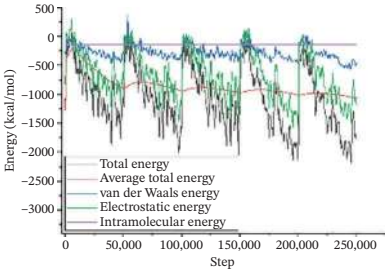
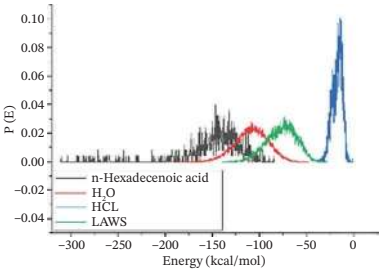
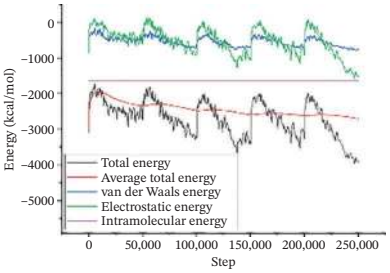
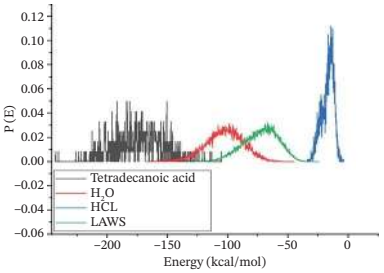
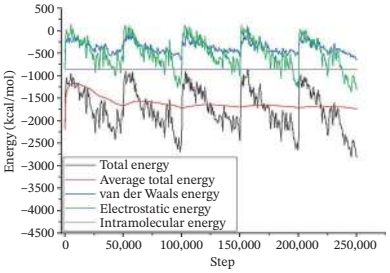
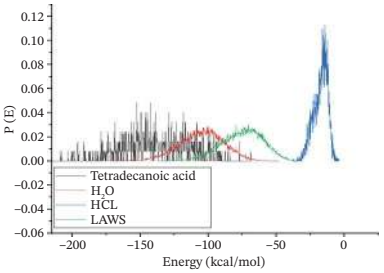
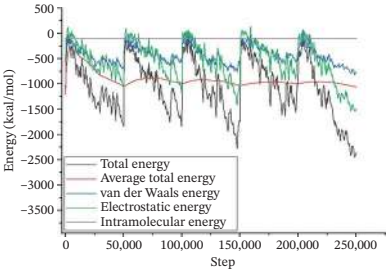
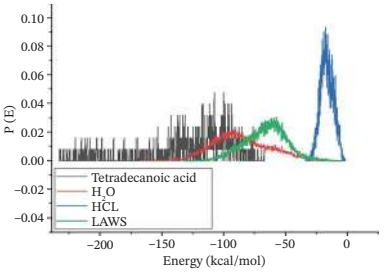
(Continues)

TABLE A7 | (Continued)

Phytochemicals	Contribution of the different energy types during the MC calculations for iron (Fe) (111)	Distribution of the adsorption energies on the iron (Fe) (111)
D-Limonene (f)		
30% Water Cut (21 H_20/9 HCl/70 LAWS system		
50% Water Cut (41 H_20/9 HCl/50 LAWS system		
70% Water Cut (61 H_20/9 HCl/30 LAWS system		
n-Hexadecenoic acid (g)		
30% Water Cut (21 H_20/9 HCl/70 LAWS system		
50% Water Cut (41 H_20/9 HCl/50 LAWS system		

(Continues)

TABLE A7 | (Continued)

Phytochemicals	Contribution of the different energy types during the MC calculations for iron (Fe) (111)	Distribution of the adsorption energies on the iron (Fe) (111)
70% Water Cut (61 H_20/9 HCl/30 LAWS system		
Tetradecanoic Acid Methyl Ester (h)		
30% Water Cut (21 H_20/9 HCl/70 LAWS system		
50% Water Cut (41 H_20/9 HCl/50 LAWS system		
70% Water Cut (61 H_20/9 HCl/30 LAWS system		

Appendix

H

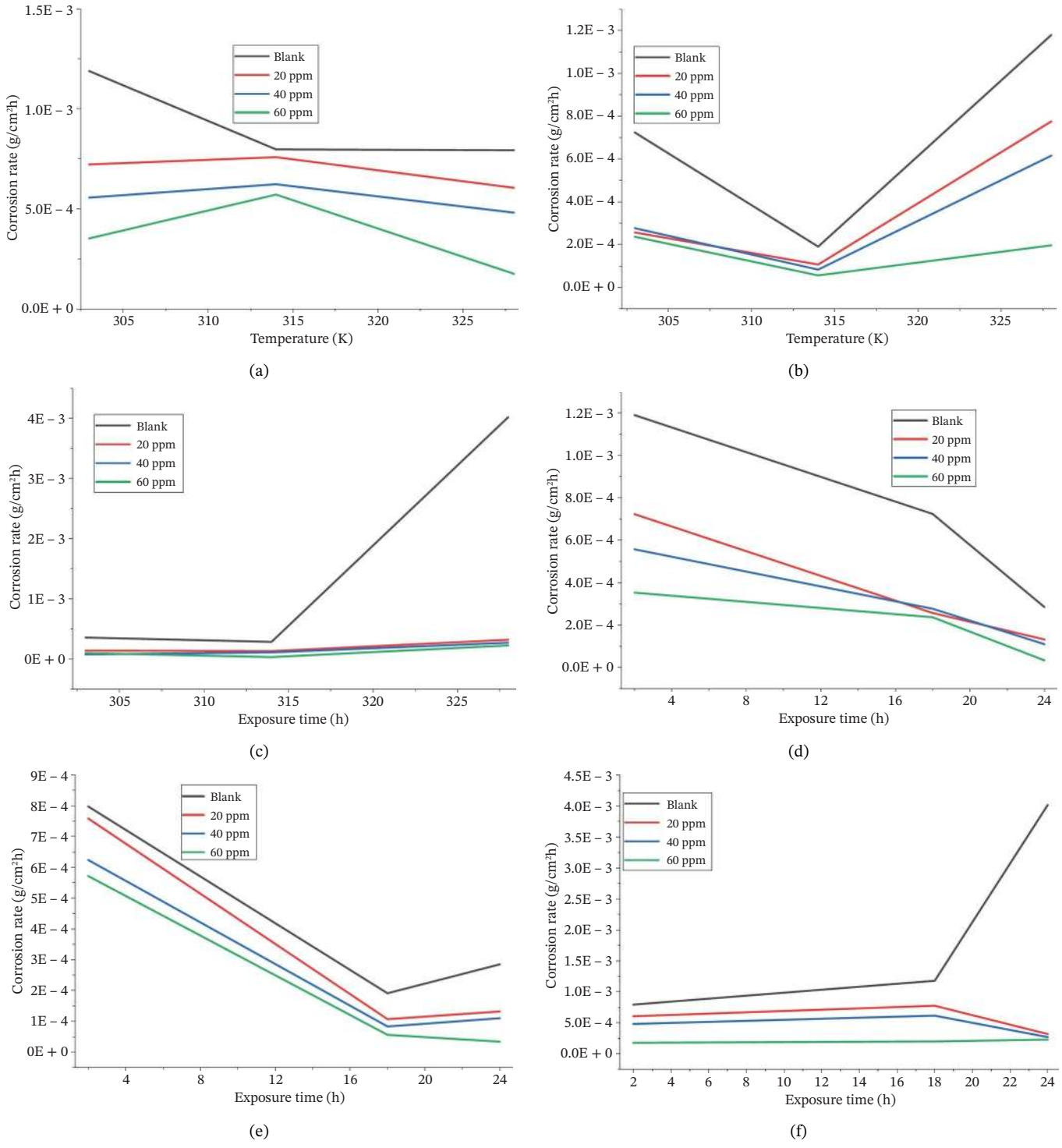


FIGURE A1 | (Continued)

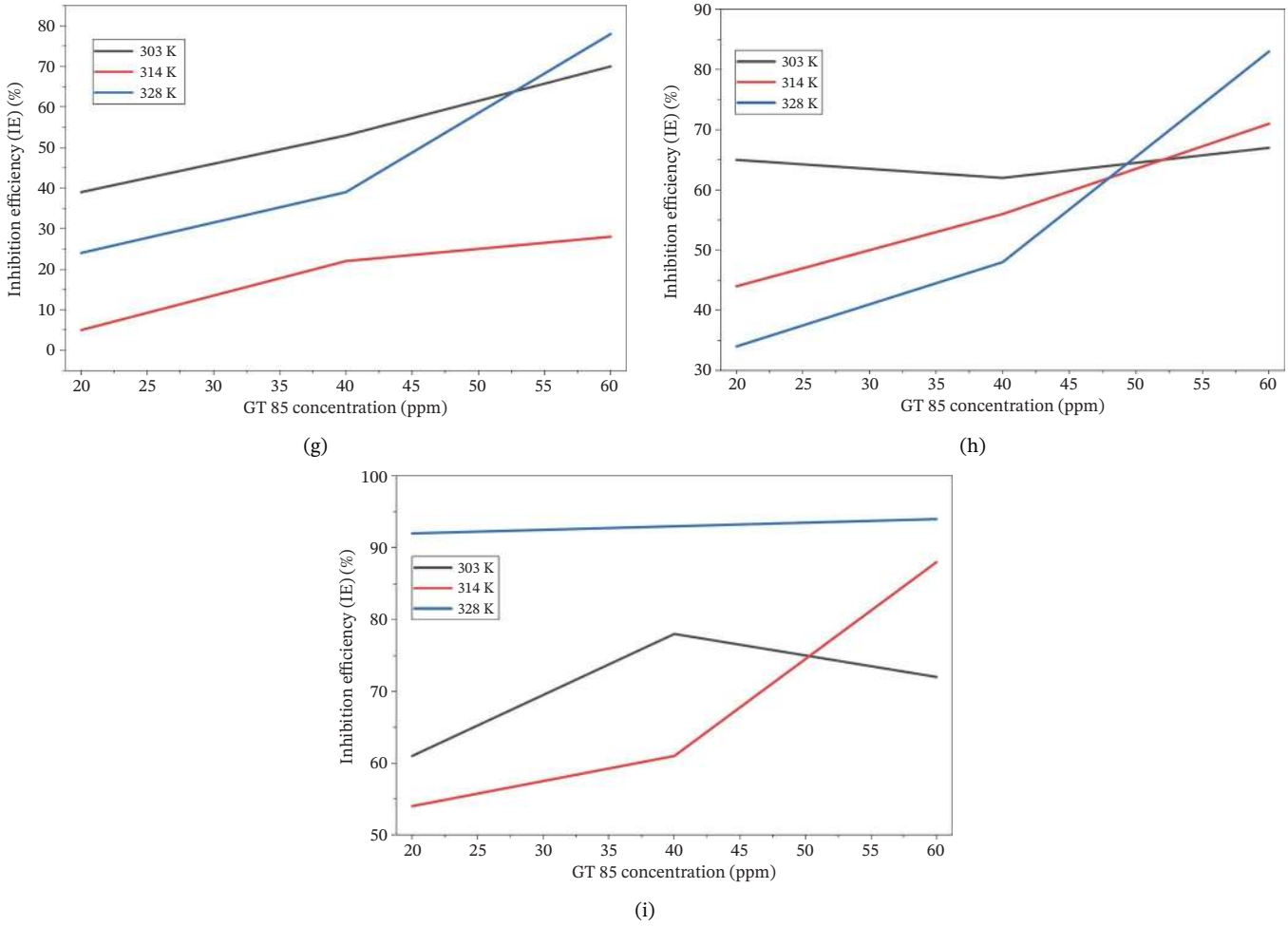


FIGURE A1 | (a–i) Effect of temperature (303, 314, and 328 K) and exposure time (2, 18, and 24 h) on corrosion rates. (a) Effect of temperatures (303, 314, and 328 K) on corrosion rate at 2 h immersion time in 0.5 M HCl. (b) Effect of temperatures (303, 314, and 328 K) on corrosion rate at 18 h immersion time in 0.5 M HCl. (c) Effect of temperatures (303, 314, and 328 K) on corrosion rate at 24 h immersion time in 0.5 M HCl. (d) Effect of exposure time (2, 18, and 24 h) on corrosion rate at 303 K in 0.5 M HCl. (e) Effect of exposure time (2, 18, and 24 h) on corrosion rate at 314 K in 0.5 M HCl. (f) Effect of exposure time (2, 18, and 24 h) on corrosion rate at 328 K in 0.5 M HCl. (g) Inhibition efficiencies at different GT 85 concentrations at varying temperatures for 2 h exposure time in 0.5 M HCl. (h) Inhibition efficiencies at different GT 85 concentrations at varying temperatures for 18 h exposure time in 0.5 M HCl. (i) Inhibition efficiencies at different GT 85 concentrations at various temperatures for 24 h exposure time in 0.5 M HCl.